

Single-photon induced instabilities in a cavity electromechanical device

Tanmoy Bera,^{1,*} Mridul Kandpal,¹ G. S. Agarwal,^{1,2} and Vibhor Singh^{1,†}

¹*Department of Physics, Indian Institute of Science, Bangalore-560012 (India)*

²*Institute for Quantum Science and Engineering,*

and Departments of Biological and Agricultural Engineering,

and Physics and Astronomy Texas A&M University, College Station, Texas 77843, USA

(Dated: May 3, 2024)

Cavity-electromechanical systems are extensively used for sensing and controlling the vibrations of mechanical resonators down to their quantum limit. The nonlinear radiation-pressure interaction in these systems could result in an unstable response of the mechanical resonator showing features such as frequency-combs, period-doubling bifurcations and chaos. However, due to weak light-matter interaction, typically these effects appear at very high driving strengths. By using polariton modes formed by a strongly coupled flux-tunable transmon and a microwave cavity, here we demonstrate an electromechanical device and achieve a single-photon coupling rate ($g_0/2\pi$) of 160 kHz, which is nearly 4% of the mechanical frequency ω_m . Due to large g_0/ω_m ratio, the device shows an unstable mechanical response resulting in frequency combs in sub-single photon limit. We systematically investigate the boundary of the unstable response and identify two important regimes governed by the optomechanical backaction and the nonlinearity of the electromagnetic mode. Such an improvement in the single-photon coupling rate and the observations of microwave frequency combs at single-photon levels may have applications in the quantum control of the motional states and critical parametric sensing. Our experiments strongly suggest the requirement of newer approaches to understand instabilities.

INTRODUCTION

Light carries momentum, and it can be used to control and manipulate the motion of a mechanical resonator down the quantum regime [1]. Such control over the motional states is essential for the technological advancement as well as to probe the fundamental physics [2, 3]. In cavity-electromechanical devices, two *linear* modes namely an electromagnetic (EM) mode and a mechanical mode are coupled with the *nonlinear* radiation-pressure interaction [1, 4]. In the microwave domain, the vibrations of the mechanical resonators are typically integrated into the EM mode using the charge modulation [5–13]. Recently, cavity electromechanical devices utilizing the magnetic-flux modulation of Josephson inductance have shown interesting results such as large electromechanical coupling rates [14–17], the near ground state cooling of the mechanical resonator by four-wave-mixing [18], and by Kerr-enhanced techniques [19]. Further, such devices have been proposed to reach the single-photon strong coupling regime using its linear scaling with the magnetic field [20–22].

Apart from providing the electromechanical coupling, the *nonlinear* nature of the Josephson inductance in flux-coupled electromechanical systems can be a valuable resource [18, 19]. It allows us to control the nature of the electromagnetic mode to change from the weak-Kerr to a single photon strong-Kerr oscillator where the response remains nonlinear down to a single-excitation. Further, under certain control parameters, the electromagnetic

(EM) mode can made to undergo a dissipative phase transition with strong fluctuations in the photon number [23]. Therefore, coupling a mechanical resonator to such an EM mode using radiation-pressure interaction offers a unique platform to study and discern the effects stemming from the *nonlinear* nature of the radiation-pressure interaction [13, 24], as well as the ones from the *nonlinear* nature of the electromagnetic mode [23].

Here, we demonstrate an electromechanical device consisting of a linear cavity, a frequency tunable transmon qubit, and a mechanical resonator [15]. First, the flux-tunability of the transmon qubit is used to implement the electromechanical coupling. Second, tuning of the transmon frequency in resonance with the cavity forms the new eigenstates due to the designed strong coupling. The anharmonicity of the resultant polariton modes can be controlled by transmon-cavity detuning [25, 26]. Such a tri-partite system thus allows us to control the electromechanical coupling and the nonlinearity of the EM mode in a single device. Therefore, by controlling the strength of the nonlinearity, the electromechanical effects can be explored as the EM mode undergoes through various regimes such as “super-splitting”, multi-photon transitions [25, 27], critical slowing down [28], photon blockade breakdown [29, 30], and transmon-ionization [31].

RESULTS

Device concept

The frequency tunable transmon qubit is enabled by a SQUID loop and a capacitor. Fig. 1a shows the schematic design of the device. The coaxial cavity is placed inside

* btanmoy@iisc.ac.in

† v.singh@iisc.ac.in

a 2-axis vector magnet, allowing us to control the axial and the normal components of the magnetic field independently. The cavity is machined from oxygen-free high conductivity (OFHC) copper. The transmon qubit is fabricated on an intrinsic-Si chip using electron beam lithography and shadow evaporation of aluminium. To achieve a larger critical in-plane magnetic field, we use 28 nm thin Al film to fabricate the device [32]. The mechanical resonator is realized by suspending one of the arms of the SQUID loop by selective isotropic dry etching of the silicon substrate. The transmon frequency can be tuned by varying the magnetic-flux through the SQUID loop.

A false color scanning electron microscope image of the SQUID loop with the suspended mechanical resonator is shown in Fig. 1b. The patterned chip is placed inside the coaxial cavity and cooled down to 20 mK in a dilution refrigerator. The details of device fabrication, and measurement setup are given in Supplementary Note 1. Since superconducting films show more resilience to the in-plane magnetic field [32], we focus on the electromechanical coupling of the out-of-plane vibrational mode of the mechanical resonator. Further, by using the control over the normal component of the magnetic field, we can cancel any out-of-plane component of the magnetic field arising from the misalignment between the axial field and SQUID plane.

Measurements

We report measurements from two similar devices but with substantially different transmon-cavity coupling rates. Detailed parameters for both the devices are listed in Supplementary Note 2. We first begin by measuring the voltage transmission $|S_{21}(\omega)|$ of Device-1 through the cavity while varying the magnetic flux through the SQUID loop. Depending on the flux passing through the SQUID loop, the transmon frequency can vary from its maximum value to a minimum value. Fig. 1c shows the color plot of the cavity transmission. As the transmon is brought in resonance with the cavity, the measured transmission splits into two well-separated dressed modes as shown in Fig. 1d, demonstrating the strong coupling. Provided low strength of the input power, the dressed cavity mode for $\Phi/\Phi_0 = 0.5$, and the vacuum Rabi-split peaks (VRS) for $\Phi/\Phi_0 = 0.27$ have the characteristic Lorentzian lineshape. From the separation of VRS, we infer the strength of the transmon-cavity coupling to be 72 MHz. The reduction in the peak height of VRS in resonant condition suggests that energy dissipation via the transmon qubit dominates over the cavity dissipation rate.

In the resonant limit of transmon-cavity, it is suitable to describe the system in terms of new eigenstates, denoted by upper and lower polariton modes with frequency ω_+ and ω_- , respectively. Away from the resonant limit, these modes exhibit a cavity-like or a transmon-like behavior with distinct anharmonicity as represented by the

gradual change of color in Fig. 1e. These polariton modes remain the flux tunability due to underlying SQUID inductance, allowing them to be utilized for implementing electromechanical interaction. Further, due to the large spectral separation between the two modes, we can analyze and describe each mode's optomechanical effect separately. Considering the upper mode, the Hamiltonian of the tri-partite system can be reduced to

$$H \simeq \omega_+ \hat{a}_+^\dagger \hat{a}_+ - \frac{K_+}{2} (\hat{a}_+^\dagger \hat{a}_+)^2 + g_+ \hat{a}_+^\dagger \hat{a}_+ (\hat{b} + \hat{b}^\dagger) + \omega_m \hat{b}^\dagger \hat{b}, \quad (1)$$

where ω_+ , K_+ , ω_m , and g_+ are the upper mode frequency, anharmonicity, mechanical frequency, and single-photon electromechanical coupling rate, respectively. The ladder operators of the upper polariton mode and the mechanical mode are denoted by \hat{a}_+ (\hat{a}_+^\dagger) and \hat{b} (\hat{b}^\dagger), respectively. The single-photon electromechanical coupling rate of the upper polariton mode can be expressed as $g_+ \simeq \xi G_+ B^\parallel l x_{zp}$, where $G_+ = d\omega_+/d\Phi$ is the flux responsivity of the upper polariton mode, B^\parallel is the axial component of the applied magnetic field, l is the length of the mechanical resonator, x_{zp} is the quantum zero-point fluctuations of the mechanical resonator and ξ is a geometrical factor of order unity and depends on the mechanical mode-shape. It is evident that higher single-photon electromechanical coupling rate can be achieved by increasing the flux-responsivity G_+ and magnetic field B^\parallel . However, the increased flux-responsivity of the dressed mode comes at a cost of reduced transmission. For the experiments discussed in the next section, we choose an operating frequency ω_+ in Device-1 that are 20 to 80 MHz detuned from the bare cavity frequency.

Cavity-enabled qubit-phonon absorption

To probe the electromechanical coupling, we use a pump-probe scheme, similar to the electromagnetically induced transparency technique [33, 34]. Fig. 2a shows the schematic of the different transitions involved in the measurement. Two coherent signals are sent to the device, *i.e.* a pump signal at a red detuned frequency ($\omega_+ - \omega_m$) which drives the $|0, m+1\rangle \leftrightarrow |+, m\rangle$ transition, and a weak probe signal at ω_p (near ω_+) to measure the transmission. We emphasize that due to the tunable nature of the polariton modes in our device, we can carry out such experiments in both low and strong anharmonicity limit, as shown in the lower panel of Fig. 2a.

We first perform the experiment in Device-1 with a ‘‘cavity-like’’ mode. Without the pump, the voltage transmission $|S_{21}(\omega_p)|$ shows the characteristic Lorentzian lineshape as shown in Fig. 2b. In the presence of the pump, an absorption feature appear in the transmission spectrum, as shown in Fig. 2c. It arises from the destructive absorption of the probe field from two different pathways [35]. The shape of the absorption feature is

determined by the response of the mechanical resonator and can be used to extract its resonant frequency and effective dissipation rate. From these measurements, we obtain the mechanical resonant frequency and linewidth to be $\omega_m/2\pi \sim 3.97$ MHz and ~ 13 Hz, respectively. In addition, we determine the single-photon coupling strength g_+ by fitting the absorption feature with an analytical expression calculated by treating the electromechanical mode as an anharmonic oscillator (Eq. S11 of Supplementary Note 3). We repeat the experiment for various pump strengths and extract the electromechanical coupling strength $g_+/2\pi \sim 40.0 \pm 2.7$ kHz, with an uncertainty arising from the statistical measurements. Since the single-photon electromechanical coupling rate is linearly proportional to the axial magnetic field B^\parallel , we carry out similar absorption experiments at different magnetic fields, and calculate the single photon electromechanical coupling rates. Fig. 2d shows the plot of experimentally determined g_+ for different values of the magnetic field.

Next, we utilize the “transmon-like” mode which exhibits a significantly larger anharmonicity compared to its dissipation rate. These measurements are done on Device-2, which is designed to have a transmon-cavity coupling of $J/2\pi \sim 193$ MHz. For the three-mode system discussed here, measurement of the transmon-phonon interaction is enabled by the cavity, we call this process cavity-enabled qubit-phonon absorption (CEQA). In the large anharmonicity limit, the absorption feature in probe transmission is shown in Fig. 2e. Due to its large anharmonicity, the CEQA feature effectively arises dominantly from the participation of ground and first excited states of the “transmon-like” mode. Consequently, we can approximate the electromechanical interaction as an effective two-level system longitudinally coupled to a mechanical resonator. Keeping this in mind, we derive an analytical expression for the absorption feature and fit the experimental data, resulting in the black line shown in Fig. 2e. Additional details pertaining to the calculations are given in the Supplementary Note 3. We emphasize that due to large g_+ in the system the CEQA feature appears in both weak and strong nonlinearity regimes down to the mean-photon occupation of $\sim 10^{-1}$ and $\sim 10^{-3}$, respectively.

Optomechanical backaction and instability

A high single-photon coupling rate results into significant optomechanical backaction at very low pump strengths. To investigate the effects of dynamical backaction on the mechanical resonator, we send a pump signal and measure the power spectral density (PSD) of the output microwave signal while varying the pump power and detuning. Depending on the pump detuning, an imbalance between the up- and down-scattering rates of microwave photons by the mechanical resonator results in its cooling or heating. We first operate at a lower

magnetic field of $B^\parallel \sim 18$ mT, and at a mode frequency of $\omega_+/2\pi \sim 5.873$ GHz, which corresponds to an estimated Kerr nonlinearity of $K_+/2\pi \sim 5.1$ MHz/photon (see Supplementary Note 2). At such operating frequency, the upper polariton mode has an estimated flux responsivity of $G_+/2\pi \sim 1.16$ GHz/ Φ_0 , and expected $g_+/2\pi \sim 13.4 \pm 0.8$ kHz (see Supplementary Note 2). Fig. 3a shows the measurements of the effective mechanical linewidth and the shift in the mechanical frequency, extracted from the PSD measurements. As expected, we observe a broadening of the mechanical linewidth for negative detunings and heating and unstable response for the positive detunings. With the increase in the strength of the pump signal, the backaction effects become enhanced, and the onset of unstable response shifts towards negative detuning due to the Kerr nonlinearity.

To theoretically understand the experimental observation, we model the system as a weak Kerr oscillator with energy decay rate $\kappa/2\pi \sim 14$ MHz, estimated from transmission spectrum. We incorporate the pump by adding a drive term in the effective Hamiltonian given by Eq. 1. To compute the backaction effects on the mechanical resonator, we solve the equations of motion for the coupled modes and obtain the expressions of the effective linewidth Γ_m and the frequency shift $\Delta\omega_m$ of the mechanical resonator (see Supplementary Note 4). The solid black lines in Fig. 3a are the theoretically calculated results.

We next focus on the unstable response of the mechanical resonator. An unstable mechanical resonator has a large oscillation amplitude, and produces a frequency comb structure in the PSD with multiple peaks separated by ω_m , as shown in Fig. 3b. In linear cavity optomechanics, such features have been studied extensively, both theoretically and experimentally [1]. We investigate the boundary of the unstable response by varying the pump power and its detuning, as shown in Fig. 3c. This experiment is carried out on Device-2, while operating at $\omega_+/2\pi \sim 5.82$ GHz, corresponding to an energy decay rate of $\kappa/2\pi \sim 9$ MHz and an electromechanical coupling rate of $g_+/2\pi \sim 45.0 \pm 1.9$ kHz, which is determined from a separate CEQA experiment. It is important to note that due to such a large coupling, the onset of mechanical instability occurs at mean photon occupation of 0.01 in the polariton mode. To theoretically understand the boundary of the instability, we use a weak-Kerr model as mentioned earlier (Supplementary Note 4), and the results from these calculations are shown by the solid-black line in Fig. 3c. By comparing the two theoretical results, we observe that due to the nonlinearity present in the system, the onset of instability shift toward lower frequencies as the pump power is increased.

Mechanical Instabilities in single-photon strong Kerr limit

We first note that the response of the circuit-QED system can be substantially different at high driving powers. Fig. 4a and b show the cavity transmission $|S_{21}|$ of Device-2 while varying B^\perp . Apart from the dominating vacuum-Rabi splitting, additional transitions arising from higher levels can also be seen. A schematic of the uncoupled and new (polariton) eigenstates is shown in the right panel of Fig. 4c. The left panel depicts the uncoupled states as $|n_c, n_q\rangle$, where n_c and n_q are the number of excitation in cavity and transmon, respectively. The symmetric and anti-symmetric combination of single excitation states $|1, 0\rangle$ and $|0, 1\rangle$ are denoted by $|+\rangle$ and $|-\rangle$, respectively. Similarly, the new eigenstates in the two-excitation manifold are labeled as $|\alpha\rangle, |\beta\rangle$ and $|\gamma\rangle$. The additional peaks in the transmission spectrum of Fig. 4b are arising from the higher-level transitions, namely $\{|+\rangle, |-\rangle\} \leftrightarrow \{|\alpha\rangle, |\beta\rangle, |\gamma\rangle\}$. Such transitions are possible with a single frequency drive due to non-zero thermal occupation of $|+\rangle$ and $|-\rangle$ states.

To identify these transitions, we treat the transmon as a nonlinear oscillator and model the system using an extended Jaynes-Cummings Hamiltonian added with a coherent drive. We then numerically solve the Markovian master equation to compute the voltage transmission. The results are plotted as solid black line in Fig. 4b. It can be seen that the transition frequencies corresponding to the peaks in the transmission spectrum match closely with the numerical results. Clearly, these transitions arise from the single photon excitation and are distinct from the multi-photon transitions [25], which usually occur at stronger drive strengths.

We next activate the electromechanical coupling by applying the parallel magnetic field $B^\parallel \sim 9$ mT. and investigate the boundary of the unstable response of the mechanical resonator in a wider span of pump power and frequency. Fig. 5a and c show the region of unstable response from Device-2 at two different values of flux-operating point, and Fig. 5b and d show the corresponding transmission spectra at $B^\parallel = 0$. For the operating flux in Fig. 5a, the transmon qubit becomes near resonant to the cavity, and the electromechanical coupling rate of the higher frequency polariton mode is estimated to reach $g_+/2\pi \sim 160$ kHz, which is nearly 4% of the mechanical mode frequency ω_m . As a consequence, the onset of mechanical instability takes place at a very low mean photon occupation of $n_d \sim 3 \times 10^{-4}$. The onset of mechanical instability coincides with the blue-detuned region of the transition frequency ω_+ and ω_- , similar to the situation in the linear cavity optomechanics. As pump power is increased, the mechanical instability emerges near the higher transition frequencies of $\omega_{-\alpha}$ and $\omega_{-\beta}$. With further increase in the pump power, we observe instabilities near the bare cavity frequency. Surprisingly, we do not see any instability branch surrounding the transition frequency $\omega_{+\gamma}$. We also note that unstable

mechanical response resulting into frequency comb features in PSD persist even beyond -5 dBm pump power. At these powers, we expect transmon to be “ionized”, and SQUID would operate in non-zero voltage regime. The cavity transmission shows the bare-cavity response as shown in the lower panel of Fig. 5b.

Fig. 5c shows similar measurements but at a different flux-operating point, such that the transmon qubit is approximately 240 MHz detuned above the cavity frequency. An instability region corresponding to single-photon transitions with frequency $\omega_{-\beta}$ and $\omega_{+\gamma}$ emerges, along with the instability branches surrounding the frequencies ω_+ and ω_- . At moderately higher power, the instability region near the two-photon transition corresponding to frequency $\omega_\gamma/2$ can be seen. We also observe the super-splitting of the ω_- peak, resulting in an abrupt widening of the instability region.

Semiclassical analysis and a model based on quantum two-level system

To gain insight into these observations, we plot the transmission measurements $|S_{21}|$ over a large frequency at $B^\parallel = 0$ and the boundary of instability, together as shown in Fig. 6a. The instability parameter-space can be divided into three regions – (i) the low-power region, where the single-photon instabilities stem from the lower transitions, (ii) the mid-power region, where higher energy single- and multi-photon transitions, super-splitting, bistability of the electromagnetic mode are important, and (iii) the “ionization” region, where the frequency-comb persists despite the SQUID operating in the non-zero voltage regime.

As the EM mode emerges from the strong coupling between the transmon and the cavity, we model it by expanding it using polariton eigenstates to capture the low-power behavior. Such an approach effectively breaks down the EM mode into independent two-level systems, which are longitudinally coupled to a mechanical resonator. Details of the model are included in the Supplementary Note 6. Results from these calculations are plotted in Fig. 6b. As expected, the theoretical model is able to capture the behavior at low pump powers, however, it does *not* capture the experimental observations at intermediate or high pump powers.

For intermediate powers, we attempt a model based on the semi-classical analysis while treating the transmon as an anharmonic oscillator (details are included in Supplementary Note 5). We first note that a driven transmon-cavity system alone (no optomechanical coupling) can have bistable and unstable solutions of the intra-cavity field [36]. We use semi-classical approach and perform the linear stability test [37]. We identify the regions with one unstable fixed-point (FP), and regions with one unstable and two stable FP, as shown in Fig. 6c. In these regions, the “intra-cavity” field is expected to show either an unstable or a bistable behavior resulting in large

photon-fluctuations.

Next, we include the optomechanical interaction, and obtain the fixed-points. The regions of the mechanical instability is shown by the dashed lines in Fig. 6c. At low powers, the semi-classical analysis could produce the mechanical instability region near the ω_{\pm} polaritons, arising from the optomechanical backaction. In addition, we note that in the optically bistable region, one of the stable solutions also give rise to mechanical instability.

Clearly, the quantum model based on the polariton-basis, and the three-mode semi-classical analysis do not capture the experimentally observed behavior. While the model based on the polariton-eigenstates captures the low-power behavior, it is not as effective in mid-power range. Particularly, in the middle part of the region (ii), the transmon-cavity system undergoes a dissipative phase transition and can take a long time to reach the equilibrium [23, 28, 30]. In this region, the presence of unstable response in the experimental data, and the absence of it in the modelled results strongly suggest the role of fluctuating photon-pressure on the mechanical resonator during the transition. These observations would require theoretical investigations beyond the standard semi-classical or two-level approach [38].

DISCUSSION

To summarize our findings, our current experiment reaches a single-photon coupling rate which is nearly 4% of the mechanical resonator frequency. It highlights that instabilities arising from the residual thermal occupations of the mechanical and EM modes would become important as one reaches the single-photon strong coupling regime $g_0 \gtrsim \{\kappa, \omega_m\}$ unless the mechanical oscillator is cooled to its quantum ground state. Single-photon strong coupling regime seem experimentally feasible as transmon qubits have been shown to operate in higher magnetic fields [32].

With such promising futuristic parameters, it is feasible to achieve ground state cooling via sideband driving below the level of a single photon, and it further suggests ways to prepare non-classical mechanical states including Schrodinger-cat [21, 22, 39]. Such methods and techniques can be extended to the low frequency flux-family superconducting qubits to realize transverse electromechanical couplings, and thus extending the toolbox available with the flux-coupled devices [40]. The generation of microwave frequency combs at single-photon level could have applications in quantum sensing [41, 42]. Our experimental observations further demand theoretical investigation into the parametric instabilities in single photon limit.

MATERIALS AND METHODS

The coaxial cavity is machined from oxygen-free high conductivity copper. The central post (solid cylinder in the lower half) has a length of 11.5 mm and diameter of 2.5 mm. The inner diameter of the outer cylinder is 5.5 mm, and the total height of the cavity is 20.5 mm. The transmon qubit is fabricated on an intrinsic silicon-(100) substrate. Using EBL and shadow evaporation of aluminum, we fabricate the device using a single step of lithography. The evaporated aluminum film is annealed under ambient conditions to transform the compressive stress to tensile stress. A selective etching of silicon is then carried out to release the nanowire (mechanical oscillator) from the substrate. To nullify the effects of annealing and etching on Josephson junction inductance, the oxidation parameter is tuned accordingly at the time of deposition so that we get the desired junction resistance at the end of all processes. Finally, the silicon chip is mounted inside the coaxial cavity and the cavity is placed inside a home-built vector magnet setup. This assembly is placed inside a double layer of infrared and magnetic field shields, and mounted to the mixing chamber plate for cooling down to 20 mK for measurements.

ACKNOWLEDGMENTS

T.B. thanks Bhoomika Bhat, Harsh Vardhan Upadhyay and S. Majumder for assisting during the device fabrication and helpful discussions. G.S.A. thanks the Infosys Foundation Chair of the Department of Physics, IISc Bangalore, which made this collaboration successful. This work is supported by the Air Force Office of Scientific Research under Award No. FA2386-20-1-4003. The authors acknowledge the support under the CoE-QT by MEITY and QuEST program by DST, Govt. of India. The authors acknowledge device fabrication facilities at CeNSE, IISc Bangalore, and central facilities at the Department of Physics funded by DST (Govt. of India).

AUTHOR CONTRIBUTION

V.S. conceived and supervised the experiment. T.B. fabricated the device and performed the measurements. T.B. and V.S. have done the data analysis. T.B., M.K., and G.S.A. carried out the theoretical calculations. All the authors have contributed in preparing the manuscript.

COMPETING INTERESTS

The authors declare no competing interests.

-
- [1] M. Aspelmeyer, T. J. Kippenberg, and F. Marquardt, *Reviews of Modern Physics* **86**, 1391 (2014).
- [2] H. Qiao, E. Dumur, G. Andersson, H. Yan, M. Chou, J. Grebel, C. R. Conner, Y. J. Joshi, J. M. Miller, R. G. Povey, X. Wu, and A. N. Cleland, *Science* **380**, 1030 (2023).
- [3] M. Bild, M. Fadel, Y. Yang, U. von Lüpke, P. Martin, A. Bruno, and Y. Chu, *Science* **380**, 274 (2023).
- [4] A. A. Clerk, K. W. Lehnert, P. Bertet, J. R. Petta, and Y. Nakamura, *Nature Physics* **16**, 257 (2020).
- [5] E. E. Wollman, C. U. Lei, A. J. Weinstein, J. Suh, A. Kronwald, F. Marquardt, A. A. Clerk, and K. C. Schwab, *Science* **349**, 952 (2015).
- [6] J.-M. Pirkkalainen, E. Damskägg, M. Brandt, F. Massel, and M. Sillanpää, *Physical Review Letters* **115**, 243601 (2015).
- [7] F. Lecocq, J. B. Clark, R. W. Simmonds, J. Aumentado, and J. D. Teufel, *Physical Review X* **5**, 041037 (2015).
- [8] D. Mason, J. Chen, M. Rossi, Y. Tsaturyan, and A. Schliesser, *Nature Physics* **15**, 745 (2019).
- [9] G. A. Peterson, S. Kotler, F. Lecocq, K. Cicak, X. Y. Jin, R. W. Simmonds, J. Aumentado, and J. D. Teufel, *Physical Review Letters* **123**, 247701 (2019).
- [10] S. Kotler, G. A. Peterson, E. Shojaei, F. Lecocq, K. Cicak, A. Kwiatkowski, S. Geller, S. Glancy, E. Knill, R. W. Simmonds, J. Aumentado, and J. D. Teufel, *Science* **372** (2021), 10.1126/science.abf2998.
- [11] E. A. Wollack, A. Y. Cleland, R. G. Gruenke, Z. Wang, P. Arrangoiz-Arriola, and A. H. Safavi-Naeini, *Nature* **604** (2022), 10.1038/s41586-022-04500-y.
- [12] Y. Seis, T. Capelle, E. Langman, S. Saarinen, E. Planz, and A. Schliesser, *Nature Communications* **13**, 1507 (2022).
- [13] S. R. Das, S. Majumder, S. K. Sahu, U. Singhal, T. Bera, and V. Singh, *Physical Review Letters* **131**, 067001 (2023).
- [14] I. C. Rodrigues, D. Bothner, and G. A. Steele, *Nature Communications* **10** (2019), 10.1038/s41467-019-12964-2.
- [15] T. Bera, S. Majumder, S. K. Sahu, and V. Singh, *Communications Physics* **4** (2021), 10.1038/s42005-020-00514-y.
- [16] P. Schmidt, M. T. Amawi, S. Pogorzalek, F. Deppe, A. Marx, R. Gross, and H. Huebl, *Communications Physics* **3**, 1 (2020).
- [17] D. Zoepfl, M. L. Juan, C. M. F. Schneider, and G. Kirchmair, *Physical Review Letters* **125**, 023601 (2020).
- [18] D. Bothner, I. C. Rodrigues, and G. A. Steele, *Communications Physics* **5**, 33 (2022).
- [19] D. Zoepfl, M. Juan, N. Diaz-Naufal, C. Schneider, L. Deeg, A. Sharafiev, A. Metelmann, and G. Kirchmair, *Physical Review Letters* **130**, 033601 (2023).
- [20] G. Via, G. Kirchmair, and O. Romero-Isart, *Physical Review Letters* **114**, 143602 (2015).
- [21] K. Khosla, M. Vanner, N. Ares, and E. Laird, *Physical Review X* **8**, 021052 (2018).
- [22] M. Kounalakis, Y. M. Blanter, and G. A. Steele, *Physical Review Research* **2**, 023335 (2020).
- [23] Q.-M. Chen, M. Fischer, Y. Nojiri, M. Renger, E. Xie, M. Partanen, S. Pogorzalek, K. G. Fedorov, A. Marx, F. Deppe, and R. Gross, *Nature Communications* **14**, 2896 (2023).
- [24] O. Arcizet, P.-F. Cohadon, T. Briant, M. Pinard, and A. Heidmann, *Nature* **444**, 71 (2006).
- [25] L. S. Bishop, J. M. Chow, J. Koch, A. A. Houck, M. H. Devoret, E. Thuneberg, S. M. Girvin, and R. J. Schoelkopf, *Nature Physics* **5**, 105 (2009).
- [26] L. S. Bishop, E. Ginossar, and S. M. Girvin, *Physical Review Letters* **105**, 100505 (2010).
- [27] S. S. Shamailev, A. S. Parkins, M. J. Collett, and H. J. Carmichael, *Optics Communications* **283**, 766 (2010).
- [28] P. Brookes, G. Tancredi, A. D. Patterson, J. Rahamim, M. Esposito, T. K. Mavrogordatos, P. J. Leek, E. Ginossar, and M. H. Szymanska, *Science Advances* **7**, eabe9492 (2021).
- [29] J. Fink, A. Dombi, A. Vukics, A. Wallraff, and P. Domokos, *Physical Review X* **7**, 011012 (2017).
- [30] R. Sett, F. Hassani, D. Phan, S. Barzanjeh, A. Vukics, and J. M. Fink, *PRX Quantum* **5**, 010327 (2024).
- [31] R. Shillito, A. Petrescu, J. Cohen, J. Beall, M. Hauru, M. Ganahl, A. G. Lewis, G. Vidal, and A. Blais, *Physical Review Applied* **18**, 034031 (2022).
- [32] J. Krause, C. Dickel, E. Vaal, M. Vielmetter, J. Feng, R. Bounds, G. Catelani, J. M. Fink, and Y. Ando, *Physical Review Applied* **17**, 034032 (2022).
- [33] M. Fleischhauer, A. Imamoglu, and J. P. Marangos, *Reviews of Modern Physics* **77**, 633 (2005).
- [34] S. Weis, R. Rivière, S. Deléglise, E. Gavartin, O. Arcizet, A. Schliesser, and T. J. Kippenberg, *Science* **330**, 1520 (2010).
- [35] G. S. Agarwal and S. Huang, *Physical Review A* **81**, 041803 (2010).
- [36] S. Khan and H. E. Türeci, *Physical Review Letters* **120**, 153601 (2018).
- [37] S. H. Strogatz, *Nonlinear Dynamics and Chaos: With Applications to Physics, Biology, Chemistry, and Engineering*, 2nd ed. (CRC Press, 2019).
- [38] F. Minganti, A. Biella, N. Bartolo, and C. Ciuti, *Physical Review A* **98**, 042118 (2018).
- [39] J. Li, S. Gröblacher, S.-Y. Zhu, and G. S. Agarwal, *Physical Review A* **98**, 011801 (2018).
- [40] B.-L. Najera-Santos, R. Rousseau, K. Gerashchenko, H. Patange, A. Riva, M. Villiers, T. Briant, P.-F. Cohadon, A. Heidmann, J. Palomo, M. Rosticher, H. le Sueur, A. Sarlette, W. Smith, Z. Leghtas, E. Flurin, T. Jacqmin, and S. Deléglise, *Physical Review X* **14**, 011007 (2024).
- [41] R. Di Candia, F. Minganti, K. V. Petrovnnin, G. S. Paraoanu, and S. Felicetti, *npj Quantum Information* **9**, 1 (2023).
- [42] S.-B. Tang, H. Qin, B.-B. Liu, D.-Y. Wang, K. Cui, S.-L. Su, L.-L. Yan, and G. Chen, *Physical Review A* **108**, 053514 (2023).

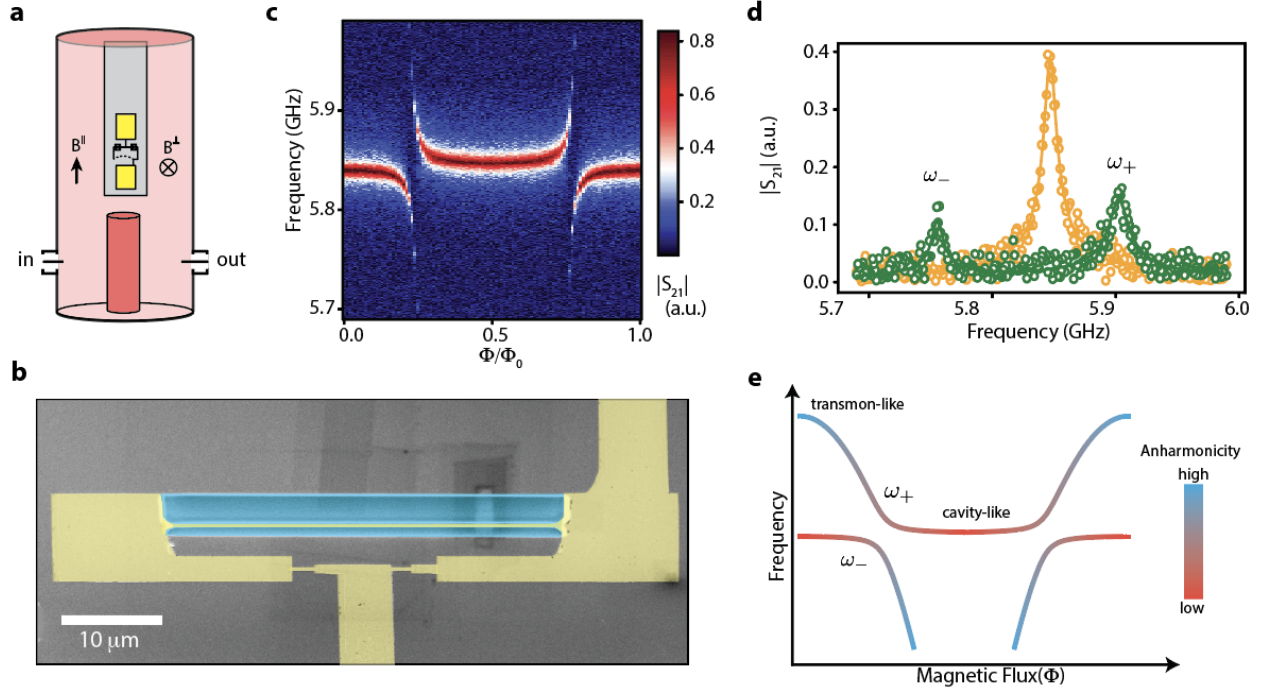


FIG. 1. **Concept:** (a) A schematic of a quarter wavelength coaxial cavity (red) coupled to a transmon (yellow). The two pads provide the shunting capacitance as well as coupling capacitance to the cavity. The axial and normal components of the magnetic-field are denoted by B^{\parallel} and B^{\perp} , respectively. (b) A tilted false-color scanning electron microscope image of the SQUID loop with embedded mechanical resonator. The suspended Al nanomechanical resonator can be seen. The Al film and the silicon substrate are shown in yellow and gray colors, respectively. The selective-etched region used to suspend the mechanical resonator is shown by the cyan-colored region. The mechanical resonator has dimensions of $40\mu\text{m} \times 200\text{ nm} \times 28\text{ nm}$. (c) A representative colorplot of the voltage transmission $|S_{21}|$ through the cavity as the magnetic flux through the SQUID loop is varied. (d) The panel shows linecut from panel (c), corresponding to $\Phi/\Phi_0 = 0.27(0.5)$ in green(yellow) emphasizing the vacuum-Rabi split peaks (dressed-cavity peak). (e) A schematic to depict the change in frequency of the dressed modes as the magnetic flux is swept. The gradual color shift from blue to red or vice versa indicates how the nonlinear character of the mode is changing with flux.

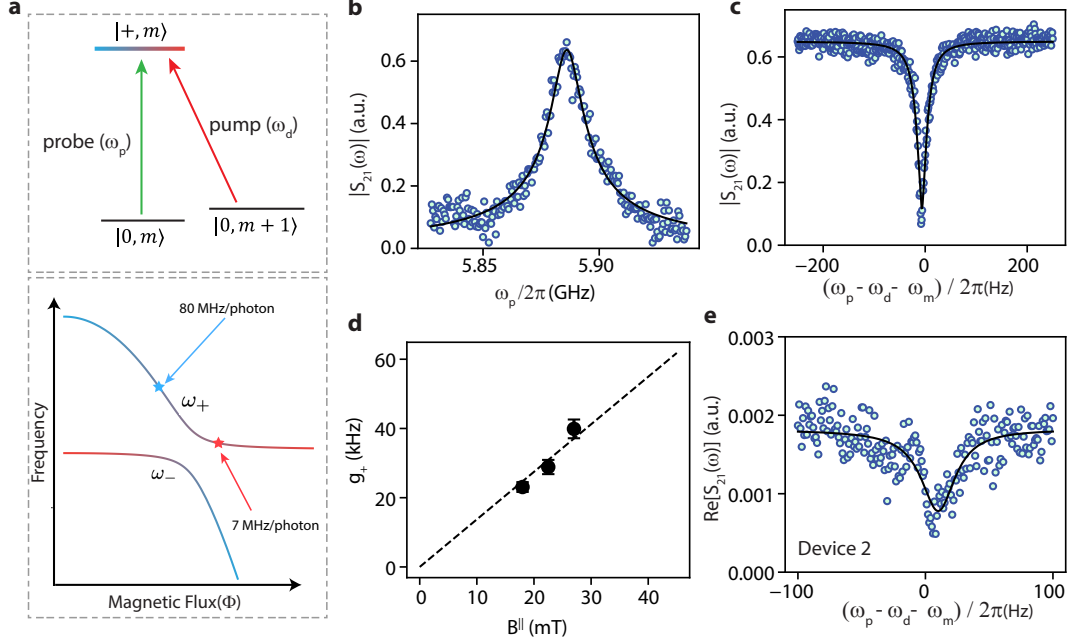


FIG. 2. Cavity-enabled qubit-phonon absorption (CEQA): (a) The top panel depicts the Pump and probe scheme for the CEQA experiment. The states $|+, m\rangle$ denote one excitation in the polariton mode, along with m excitations in the mechanical resonator. The pump and probe signals are shown by the red and green arrows, respectively. The lower panel schematically illustrates operating points for the CEQA experiment in both devices. The red star represents the operating point in Device-1, indicating weak nonlinearity in the polariton mode, whereas the blue star represents the operating point in Device-2, indicating strong nonlinearity. (b) Measurement of $|S_{21}|$ in the absence of the pump signal, showing the linear response of the polariton mode. The solid-black line is a Lorentzian fit to the response. (c) In the presence of a pump signal, an absorption feature appears in the probe transmission. At $B_{||} \sim 27$ mT, the polariton mode frequency is set to $\omega_+/2\pi \sim 5.884$ GHz. The applied pump strength is $P_i = -19$ dBm, which corresponds to mean “photon” occupation of $(5.80 \pm 0.07) \times 10^{-2}$, and the probe signal is 6 dB smaller than the pump. The solid black curve is the fitted curve yielding a single-photon coupling rate $g_+/2\pi \sim 40.0 \pm 5.5$ kHz. (d) Experimentally determined g_+ for three different values of the applied magnetic field $B_{||}$. While increasing $B_{||}$, the flux-responsivity is nominally kept constant by adjusting B_{\perp} . (e) The absorption feature arising in the probe transmission of a strongly nonlinear mode in Device-2. The mode frequency is chosen to be $\omega_+/2\pi \sim 6.005$ GHz, which corresponds to a qubit detuning of $(\omega_q - \omega_c)/2\pi \sim 120$ MHz. An analytical formula derived from a two-level system coupled to a mechanical resonator is used to fit the data, yielding the solid black curve.

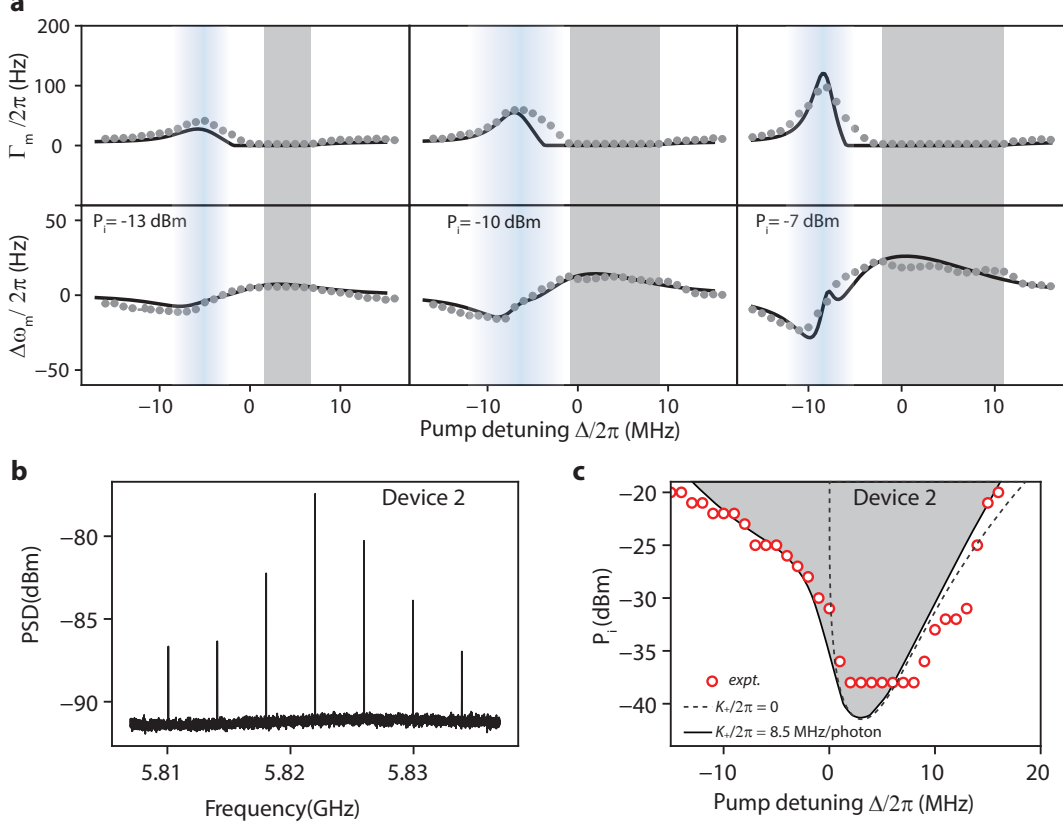


FIG. 3. Dynamical backaction on the mechanical resonator: (a) Measurements from Device-1. Total mechanical linewidth and change in the mechanical frequency extracted from the power spectral density (PSD) measurements as the pump detuning is varied at a constant pump power. From left to right panels, the pump power is increased. For these measurements, the dressed mode is tuned to $\omega_+/2\pi \sim 5.873$ GHz and the axial magnetic field is set to $B^\parallel \sim 18$ mT, resulting in an electromechanical coupling rate of $g_+/2\pi \sim 13.4 \pm 0.8$ kHz. The solid-black lines are the results of the theoretical calculations based on a Kerr-like oscillator model. The blue-color gradient and gray-shaded region denote the cooling and unstable response of the mechanical resonator. (b) PSD of the output microwave signal showing the formation of the frequency combs when the mechanical resonator becomes unstable. The peaks are separated by ω_m . The measurement is performed using a resolution bandwidth of 5 kHz. (c) The boundary of the mechanical instability in the parameter space of the pump detuning and power. These measurements are carried out on Device-2 with polariton mode frequency $\omega_+/2\pi \sim 5.82$ GHz, and applied magnetic field $B^\parallel \sim 9$ mT, which resulted in $g_+ \sim 45 \pm 2.7$ kHz. The dashed line is the theoretical prediction based on a linear oscillator model (zero Kerr nonlinearity) with the same electromechanical coupling.

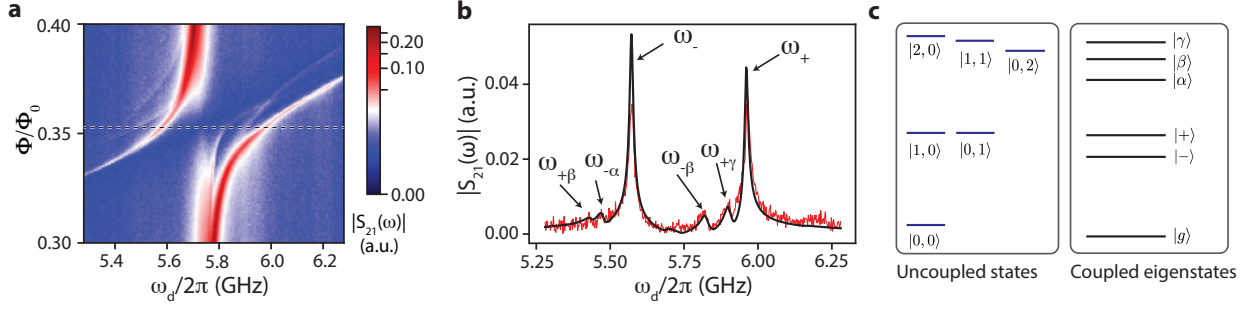


FIG. 4. **Higher-energy single-photon transitions of transmon-cavity system:** (a) Colorplot showing the voltage transmission $|S_{21}(\omega)|$ through the cavity for Device-2 at relatively stronger probe. To suppress effects arising from the electromechanical interaction, no B^\parallel is applied. (b) A linecut from $|S_{21}|$ measurement shown in panel-(a) at the position shown by the dashed line. A small B^\perp is used to tune transmon frequency while B^\parallel is kept at zero. The solid line is the result from numerical calculations, while considering a small thermal population in both transmon and cavity modes. Peaks are marked according to the transition frequencies. (c) Left panel shows the energy levels of uncoupled states of the transmon-cavity system. The right panel depicts energy-eigenstates resulting from the strong coupling.

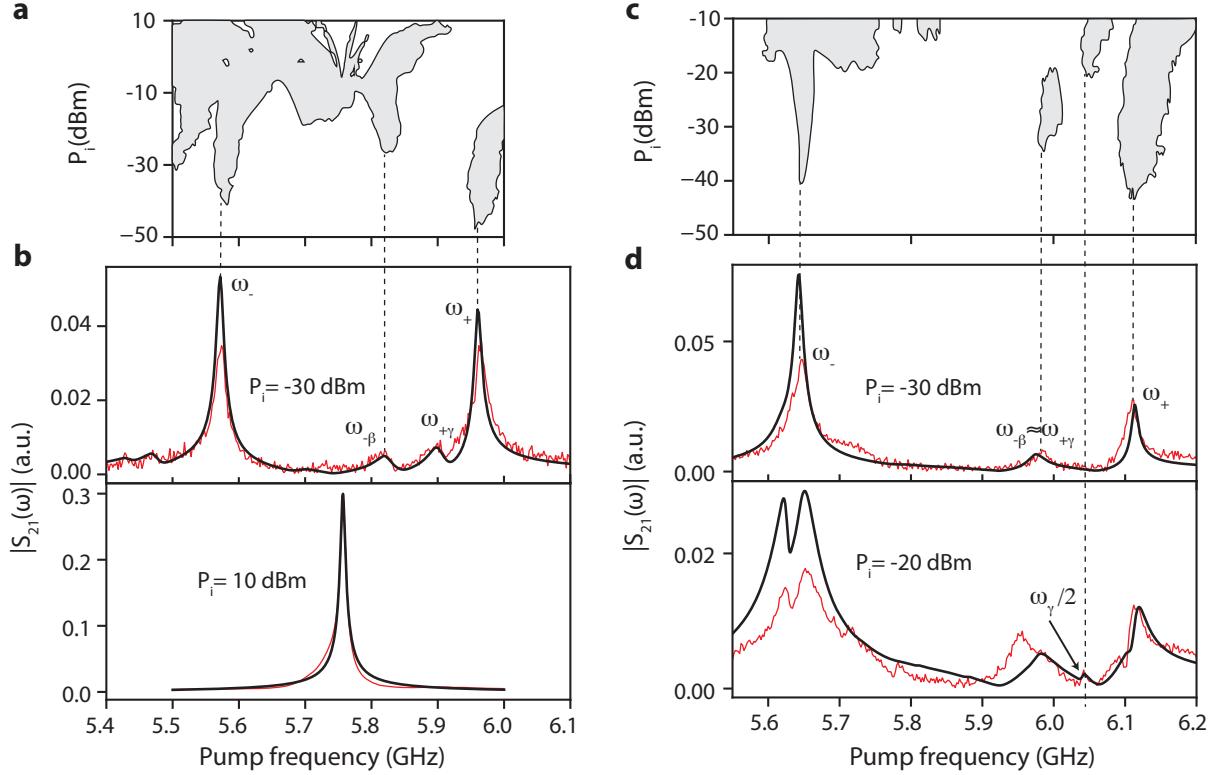


FIG. 5. **Mechanical instabilities due to single-, multi-photon transitions and super-split vacuum Rabi mode:** (a, c) show the regions of the mechanical instability in gray color as pump power P_i and frequency ω_d are varied. The measurements are carried out on Device-2 at two different flux bias points corresponding to $(\omega_q - \omega_c)/2\pi \sim 40$ MHz, and 240 MHz. (b, d) show the transmission of the cavity at two different drive powers at $B^\parallel = 0$ mT. The black lines represent the results of the numerical calculations that took into consideration transmon qubit's anharmonicity and treat it as a Kerr oscillator. The numerical calculations capture the transition frequencies, however it does not capture the shape accurately presumably due to power dependent relaxation and dephasing rates of transmon. The dotted-lines are drawn as a guide for the eye to connect to the instability onset points in panel (a,c).

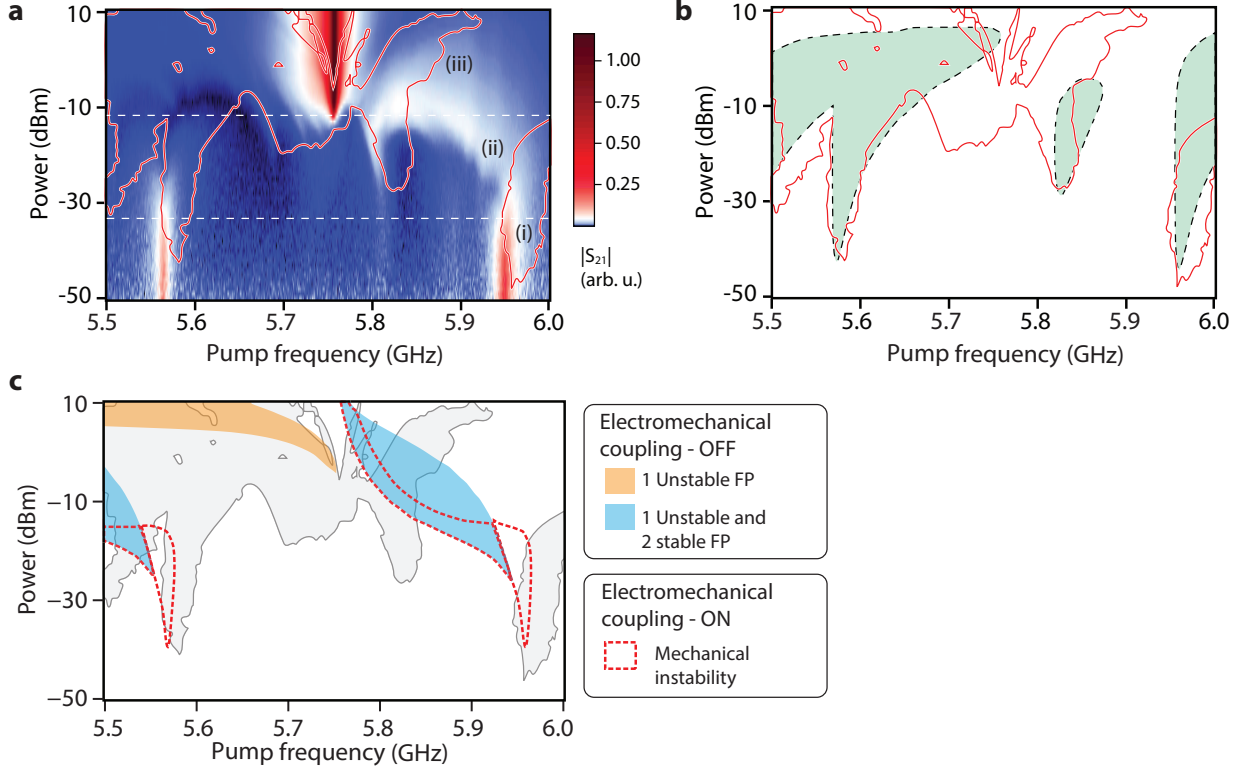


FIG. 6. **Insights into the instability region:** (a) Transmission $|S_{21}(\omega)|$ of Device-2 as the pump power is varied. For a direct comparison with the various transitions relevant at high powers, the boundary of instability region (as shown in Fig. 5(a)) is plotted on the top (red curve). (b) The region with light green color shows the mechanical instability computed by modeling the electromagnetic mode using polariton eigenstates, while considering their individual coupling to the mechanical mode with varying strengths. For comparison, the boundary of the instability is replotted (red curve). Panel (c) summarizes the results from semi-classical analysis of the system. It shows different regions with one or more stable and unstable FP when the optomechanical coupling is set to zero. Region of mechanical instability due to optomechanical backaction for the stable FPs of the system is also included. The experimental boundary of mechanical instability is plotted in light-gray color.

SUPPLEMENTARY NOTE 1.

A. Device Fabrication and experimental setup

The devices are fabricated on a cleaned $2.5 \text{ mm} \times 7 \text{ mm}$ silicon-(100) substrate. A single-step electron beam lithography (EBL) process is used to pattern the substrate with a bi-layer resist stack of MMA-EL-11 and PMMA-950-A4. Subsequently, aluminum(Al) films are deposited using shadow evaporation technique with an intermediate *in-situ* oxidation step. We found the evaporated films to be under compressive stress after the deposition, which is not quite suitable for the release of the Al-resonator. To convert it to the tensile stress, the chip is annealed at 180°C for 15 min in the ambient environment. It leads to a change in the tunnel junction resistance of the SQUID at room temperature, as mentioned in Table S1.

Next, we carry out electron beam lithography using a single layer of PMMA resist and pattern a rectangular window surrounding the nanowire. It is followed by a reactive ion etching (RIE) process, where the silicon underneath the wire is etched out. The etching process is done in two steps, using SF_6 gas only. In the first step, silicon is anisotropically etched by using a low process pressure ($\approx 9 \text{ mTorr}$). It is then followed by an isotropic etch at higher process pressure ($\approx 95 \text{ mTorr}$). The isotropic etch step removes silicon underneath the nanobeam and makes it suspended. Without breaking the vacuum, PMMA ashing is carried out to remove any residual resist on the substrate. Fig. S1(a) shows the optical image of the qubit fabricated on the silicon chip.

The etching process further affects the tunnel resistance of the junctions. We have consistently seen a reduction in the tunnel resistance by 40 – 45% while annealing the substrate and an increase in the resistance by 15 – 20% after the etching process. To accomodate these changes, the oxidation parameters during the junction fabrication are tuned to get the target junction resistance after the final step.

Finally, the chip is placed inside a coaxial cavity, and then inside a home-built vector magnet setup. We use two layers of concentric shielding cans to protect the device from the infrared radiation and stray magnetic field. The radiation tight inner can is coated with an IR absorbing layer, and the outer can is made of cryo-perm, which helps in reducing the magnetic field fluctuations at the sample. The entire assembly, mounted to the mixing chamber plate of dilution refrigerator is shown in Fig. S1(b). Fig. S1(c) shows the schematic of the complete measurement setup used in the experiment.

B. Derivation of the single-photon coupling rate

The single-photon electromechanical coupling rate is defined as the change in resonance frequency due to the zero point fluctuation of the mechanical resonator. For

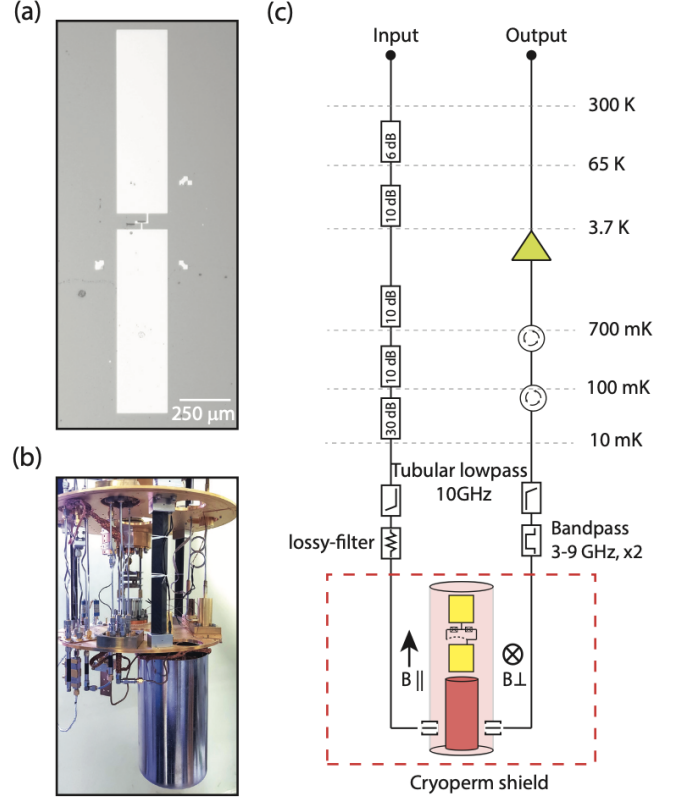


FIG. S1. **Device details and the measurement setup:** (a) An optical microscope image of the qubit device patterned on a silicon substrate. The white rectangles are the qubit antenna pads. In between the pads, a SQUID loop with a suspended nanowire is patterned. (b) Entire device assembly, inside a two-layer shield, attached to the mixing chamber plate of the dilution refrigerator is shown. (c) Schematic of the measurement setup, showing input and output lines with the attenuation, amplifier, and filters.

the upper polariton mode, it can be written as

$$g_+ = \frac{d\omega_+}{dx} x_{zpf} = \frac{d\omega_+}{d\Phi} \frac{d\Phi}{dx} x_{zpf} = G_+ \frac{d\Phi}{dx} x_{zpf}, \quad (\text{S2})$$

where $G_+ = d\omega_+/dx$ is the flux responsivity, and Φ is the total magnetic flux passing through the SQUID loop. The magnetic-flux Φ through the SQUID loop can be written as

$$\Phi = \vec{B} \cdot \vec{A} = B_{\perp} l(w + a \cdot x_{\parallel}) + B_{\parallel} l a x_{\perp}.$$

The first-term comes due to the out-of-plane magnetic field. It has a static component and a component arising from in-plane motion x_{\parallel} of the suspended nanowire. The second term originates from the out-of-plane motion of the beam x_{\perp} and the in-plane magnetic field. Upon substitution in Eq. S2, we get

$$g_+ = B_{\perp} l x_{zpf} + B_{\parallel} l x_{zpf}. \quad (\text{S3})$$

Here we have assumed that in-plane and out-of-plane mode of vibrations are nearly degenerate and therefore

results in the same vacuum zero-point fluctuations x_{zpf} . Since $B_{\parallel} \gg B_{\perp}$, the first term can be ignored.

SUPPLEMENTARY NOTE 2.

A. Device Parameter tables

Device-1	Symbol	Value
Cavity frequency	$\omega_c/2\pi$	5.846 GHz
Bare cavity decay rate	κ_b	8 MHz
Maximum qubit frequency	$\omega_q^0/2\pi$	7.38 GHz
Qubit-cavity coupling rate	$J/2\pi$	72 MHz
Measured transmon anharmonicity	$-\alpha_T/2\pi$	-284 MHz
Tunnel resistance after deposition	R_n	8.9 k Ω
Tunnel resistance after annealing	R_n	5 k Ω
Tunnel resistance after etching	R_n	5.9 k Ω
Josephson inductance of SQUID	L_J	7 nH
Mechanical resonator length	l	$\sim 40 \mu\text{m}$
Mechanical resonator width	b	$\sim 250 \text{ nm}$
Mechanical resonator thickness	d	$\sim 28 \text{ nm}$
Mass of the mechanical resonator	m	$\sim 0.75 \text{ pg}$
Mechanical resonator frequency	$\omega_m/2\pi$	$\sim 3.97 \text{ MHz}$
Maximum axial magnetic field	B_{max}	$\sim 45 \text{ mT}$
Product of input-line attenuation and input coupling rate	A/κ_{in}	$\sim 17444 \text{ s}$

TABLE S1. Summary of the key parameters of the first sample studied.

Device-2	Symbol	Value
Bare cavity frequency	$\omega_c/2\pi$	5.744 GHz
Bare cavity decay rate	κ_b	8 MHz
Maximum qubit frequency	$\omega_q^0/2\pi$	8.26 GHz
Qubit-cavity coupling rate	$J/2\pi$	193 MHz
Measured transmon anharmonicity	$-\alpha_T/2\pi$	-300 MHz
Mechanical resonator length	l	$\sim 40 \mu\text{m}$
Mechanical resonator width	b	$\sim 250 \text{ nm}$
Mechanical resonator thickness	d	$\sim 28 \text{ nm}$
Mass of the mechanical resonator	m	$\sim 0.75 \text{ pg}$
Mechanical resonator frequency	$\omega_m/2\pi$	$\sim 3.97 \text{ MHz}$
Maximum axial magnetic field	B_{max}	$\sim 9 \text{ mT}$
Product of input-line attenuation and input coupling rate	A/κ_{in}	$\sim 1647 \text{ s}$

TABLE S2. Summary of the key parameters of the second sample studied.

Table S1 and S2 list the parameters of the devices used in the experiment.

B. Calibration of input-line attenuation

To estimate the total attenuation in the input line, we use the ac-stark shift measurement. We tune the dressed transmon frequency of Device-1 to $\omega_q/2\pi \sim 5.325 \text{ GHz}$ where it couples dispersively to the cavity. Using the

two-tone spectroscopy technique, we measure the transmon qubit spectrum while probe power is varied. With the increase in probe power, the qubit transition frequency shifts, and it is given by $\omega_q' = \omega_q - 2n_d\chi$, where n_d and χ are mean intracavity probe photon occupation and the dispersive shift of the qubit, respectively. The dispersive shift is given by $\chi = -\frac{J^2}{\Delta} \frac{\alpha_T}{\Delta - \alpha_T}$, where $\Delta = \omega_q - \omega_c$ is the detuning between qubit and cavity. In a separate measurement, we estimate the dispersive shift $-3.5 \pm 0.126 \text{ MHz}$ of the qubit. The experimentally computed intracavity photon $(\omega_q' - \omega_q)/2\chi$ is plotted with the input probe power in Fig. S2(a). Thus, it allows us to estimate the product of the total input line attenuation and the coupling rate of the input port for Device-1. The same procedure was carried out for Device-2 as well. The estimated attenuation for both devices is given in Table S1 and S2. This parameter allows us to calculate the mean photon occupancy in a mode for a specific pump power and energy decay rate of the mode.

C. Calibration of the net output gain

To calibrate the net output gain, we send a pump signal at frequency ω_+ and record the transmitted power P_d at the same frequency. The Inset of Fig. S2(b) shows the measured power spectral density (PSD) recorded using a spectrum analyzer. The transmitted power at pump frequency is given by $P_d/\hbar\omega_+ = A_P n_d \kappa_e$, where A_P is the net output power gain, n_d is the mean occupation of the EM mode due to the coherent pump, and κ_e is the coupling rate of the output port. We vary the pump signal strength and measure P_d in a spectrum analyzer. Using the input line attenuation, given in the device parameter table, and the dressed mode decay rate of $\kappa/2\pi \sim 9.7 \pm 0.1 \text{ MHz}$, we can estimate the mean photon occupation n_d for all pump powers. The measured P_d is then plotted against the mean dressed mode occupation n_d , as depicted in Fig. S2(b). From the slope of the linear fit, we estimate the net gain. Using the output coupling rate of $\kappa_e/2\pi \approx 6.2 \text{ MHz}$ (discussed in the following section) the net gain of the output line is estimated to be $A_P = 58.5 \text{ dB}$. The same exercise is carried out in Device-2 as well, resulting in a net gain of $A_P = 64.3 \text{ dB}$. The net gain of the output line can be used to estimate mean-photon occupancy n_d of the mode, using $n_d = P_d/(A_P \kappa_e \hbar\omega)$. The reported mean-photon occupation for the experimental result shown in Fig.5(a) of the main text is determined from this method.

D. Estimation of the effective mechanical mode temperature

A pump signal, tuned to the dressed mode frequency ω_+ produces two sidebands at $\omega = \omega_+ \pm \omega_m$ due to the thermal motion of the mechanical resonator. The output microwave power spectral density (PSD) of the sideband

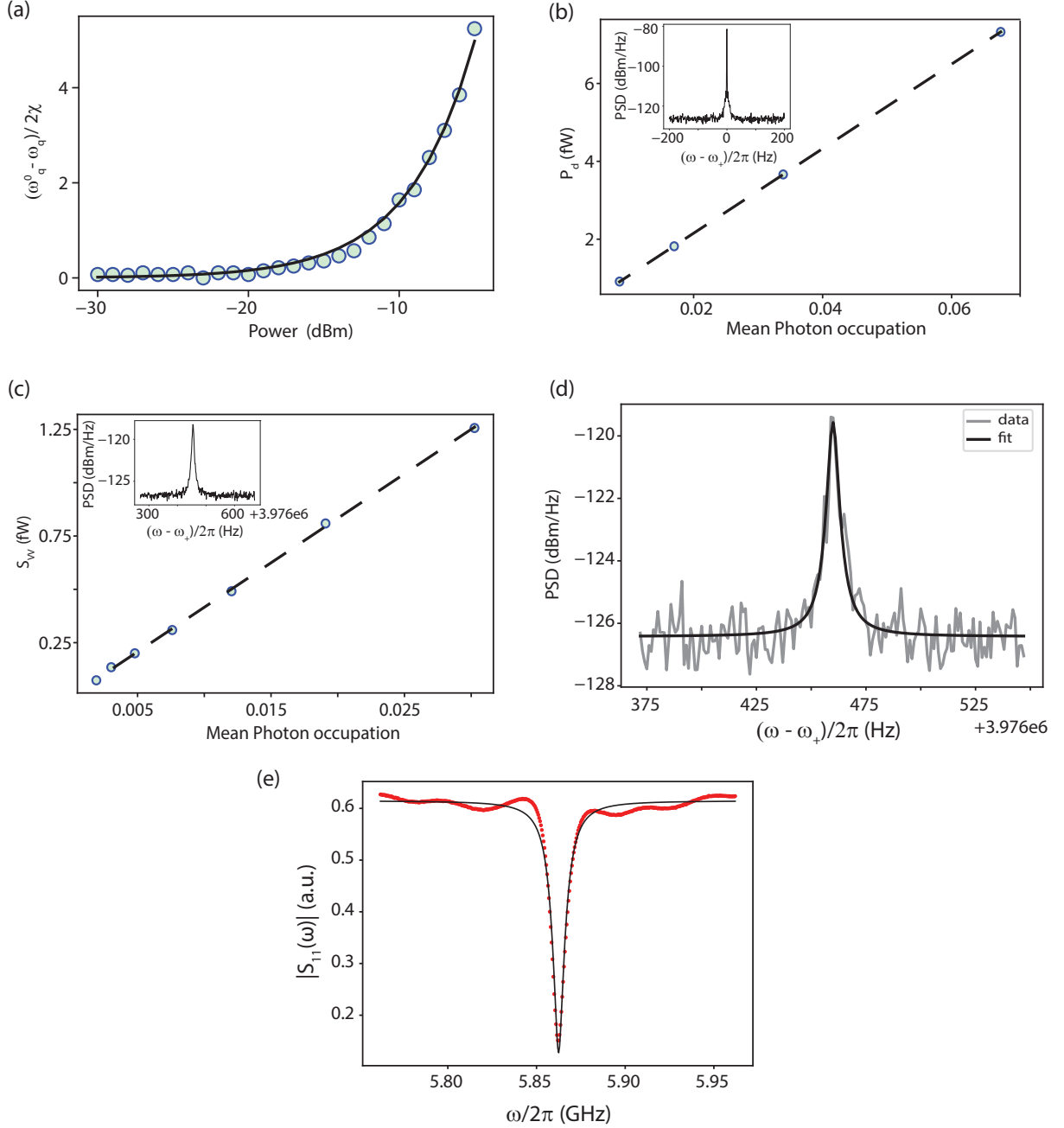


FIG. S2. All results are from Device-1. (a) Plot of the experimentally determined mean photon occupation with the input probe power. The data points show the normalized shift in the qubit frequency while performing *ac*-Stark shift measurement. The solid black line is the fit that relates the injected microwave power to the mean photon occupation of the cavity. (b) Plot of the transmitted power P_d at ω_+ with mean dressed-mode occupation n_d . The dashed line is the linear fit and its slope is used to estimate the net output gain. This measurement is carried out at a mode frequency of 5.864 GHz and applied magnetic field of $B^{\parallel} \sim 18$ mT. The inset shows the output signal, recorded using a spectrum analyzer, when a pump signal at ω_+ is injected into the device. (c) The output microwave power at the sideband peak S_{VV} is plotted with mean dressed mode occupation. The dashed line is a linear fit, and its slope is used to estimate mean thermal phonon occupation. Inset of (c) shows the mechanical resonator's spectrum. It is the power spectral density (PSD) of the lower mechanical sideband for a pump at ω_+ . (d) PSD of the mechanical resonator when axial magnetic field is 18 mT, and dressed mode frequency is 5.864 GHz. From the Lorentzian fit (black-line) to the data, we estimate the mechanical resonator frequency $\omega_m/2\pi \sim 3.97$ MHz and intrinsic linewidth $\gamma_m/2\pi \sim 6$ Hz. (e) Reflection measurement from the output coupling port at a temperature of 1 K. The black line is from the fitted model.

peak is given by,

$$\frac{S_{VV}}{\hbar\omega} = A_P \left(\frac{1}{2} + n_{add} + \frac{k_e}{\gamma_m} \frac{16g_+^2 n_d n_m}{(k^2 + 4\omega_m^2)} \right).$$

We pump the dressed mode at zero detuning and record the PSD of the lower mechanical sideband using a spectrum analyzer. In the inset of Fig. S2(c), we show a representative measurement of the microwave PSD showing the mechanical mode. Fig. S2(c) shows the plot the microwave output power at the sideband peak $S_{VV}(\omega_+ - \omega_m)$ with the mean pump photon occupation n_d in the dressed mode. From the slope of a linear line fit, we estimate the mean thermal occupation n_m of the mechanical resonator. The dressed mode frequency is tuned to $\omega_+/2\pi \sim 5.884$ GHz and axial magnetic field $B_{\parallel} \sim 18$ mT is applied. These parameters correspond to an electromechanical coupling of $g_+/2\pi \sim 22$ kHz, which is measured separately in CEQA experiment as described in the main text. The dressed mode decay rate $\kappa/2\pi \sim 11.5 \pm 0.3$ MHz is extracted from transmission $|S_{21}(\omega)|$. With all these parameters, we estimate the thermal phonon occupation of the mechanical resonator to be $n_m \sim 365$, which corresponds to a mode temperature of 70 mK.

E. Mechanical resonator's linewidth in lower magnetic fields

The mechanical resonator's linewidth of 13 Hz, reported for the Device-1 in the main text is affected by the flux noise present in the system. To mitigate this effect and find out the intrinsic mechanical linewidth, we record the output mechanical PSD of the pump while operating at a smaller magnetic field ($B_{\parallel} \sim 18$ mT), an operating point with the lower flux responsivity of the polariton mode ($G_+/2\pi = 0.55$ GHz/ Φ_0), and a low pump strength to avoid any backaction.

Fig. S2(d) shows the PSD of the lower mechanical sideband for a pump signal sent at $\omega_+/2\pi \sim 5.864$ GHz. By doing a Lorentzian fit on the spectrum, we determine the intrinsic linewidth of $\gamma_m/2\pi \sim 6$ Hz.

F. Estimation of the output coupling rate

To estimate the coupling rate of the output port with the cavity, we measure the port's reflection $|S_{11}(\omega)|$ at 1 K temperature. The reflection measurement is done in a separate cooldown where a 20-dB direction coupler is added to the output line. The cable between the output port of the cavity and the directional coupler creates small ripples in the reflected signal which can be seen in Fig. S2(e).

We fit the data to model

$$S_{11}(\omega) = 1 - \frac{\kappa_e}{(\kappa_i + \kappa_{in} + \kappa_e)/2 + i(\omega - \omega_c)},$$

where κ_i is the internal cavity decay rate, κ_{in} is the input-port coupling rate, ω_c is the cavity resonance frequency and κ_e is the output-port coupling rate. From the fit, we estimate the output coupling rate to be $\kappa_e/2\pi \sim 6.2 \pm 0.1$ MHz.

G. Flux-responsivity and Kerr-nonlinearity of the dressed mode

From the cavity transmission $|S_{21}(\omega)|$ near the vacuum Rabi splitting, as shown in Fig. 1(d) of main text, we can calculate the flux responsivity of the dressed mode for both devices. First, we estimate the mode frequency ω_+ at each flux bias point by fitting a Lorentzian to $|S_{21}(\omega)|$ measurement. Subsequently, the extracted results can be used to numerically compute the first derivative of ω_+ with respect to flux bias (Φ), i.e., the flux responsivity. In Fig. S3, we plot G_+ of the upper dressed mode with the mode frequency.

The flux responsivity can be utilized to estimate the coupling rate at different flux bias points, employing straight forward relation $g_+ = G_+ B_{\parallel} x_{zpf}$. This method is particularly useful for determining coupling rates for mode frequencies not determined by CEQA experiment. From the CEQA experiment in Device-1 (Fig. 2(d) of main text), we know that $g_+/2\pi \approx 23.1 \pm 1.4$ kHz for dressed mode frequency of 5.884 GHz when B_{\parallel} was set to 18 mT. From this known value of coupling strength, we estimate g_+ at dressed mode frequency of 5.873 GHz to be 13.4 ± 0.8 kHz, which is used to compute the black curves in Fig. 3(a) of the main text.

Next, we try to estimate the Kerr nonlinearity of the dressed modes. Using the QuTip package[1], we compute the eigen-energies of the system while varying the transmon qubit frequency. The system Hamiltonian is defined using the device parameters given in Table. S1 and S2. Subsequently, we estimate the Kerr nonlinearity of the dressed mode by calculating the difference between different energy levels, and the result is plotted in red curve of Fig. S3.

For the numerical calculations of the Kerr nonlinearity, we model the transmon and cavity as a 4-level systems each. For the numerically calculated plot of Fig. 4(b) in the main text, the Hilbert space dimension is chosen to be 9, consisting of 3-levels of transmon and 3-levels of the cavity. The mean-thermal occupation is set to be 0.1 for both transmon and cavity, which is essential to capture the higher transitions. These values are also used to compute the plots in Fig. 5(b) and (d) of the main text.

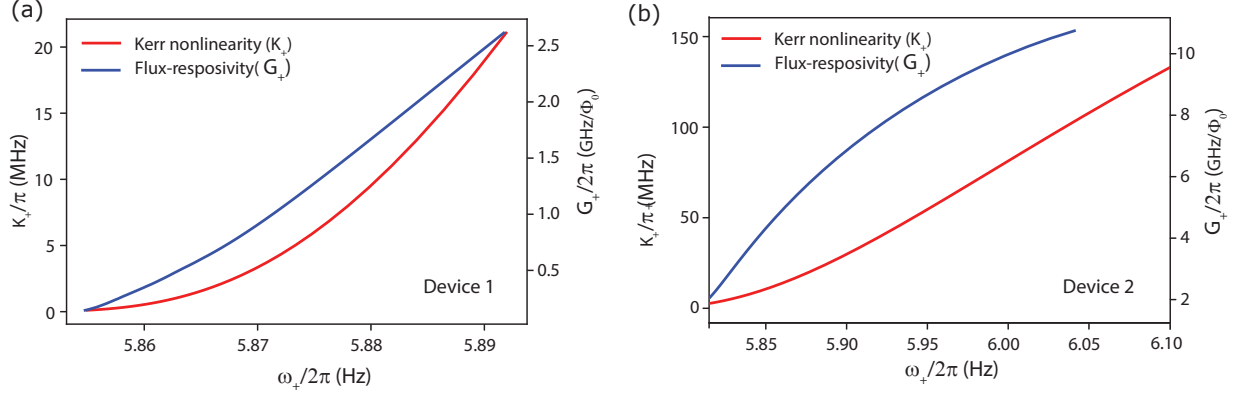


FIG. S3. Plot of the flux responsivity (G_+) and Kerr nonlinearity (K_+) of the upper polariton mode for Device-1 and Device-2 are shown in (a) and (b), respectively. G_+ is extracted from the direct cavity measurements. The anharmonicity of the polariton mode $|K_+|$ is numerically calculated using QuTip[1] and the experimentally determined device parameter given in the device parameter Table.

SUPPLEMENTARY NOTE 3.

A. Modeling of cavity-enabled qubit-phonon absorption

1. In weak anharmonicity limit

For the experiment discussed in Fig. 2(c) of main text, the transmon-cavity detuning is kept such that the polariton mode's decay rate is larger than its anharmonicity. In this limit, the upper-polariton mode can be treated as a weak-Kerr oscillator. Hence, only considering the upper polariton mode, the system can be described as a weak-Kerr oscillator of frequency ω_+ longitudinally coupled to a mechanical resonator of frequency ω_m . In the presence of two continuous drive signals, a strong pump and a weak probe, the Hamiltonian of the system can be written as

$$H = \omega_+ \hat{a}_+^\dagger \hat{a}_+ - \frac{K_+}{2} \hat{a}_+^\dagger \hat{a}_+^\dagger \hat{a}_+ \hat{a}_+ + \omega_m \hat{b}^\dagger \hat{b} + g_+ \hat{a}_+^\dagger \hat{a}_+ (\hat{b} + \hat{b}^\dagger) + \epsilon_d (\hat{a}_+ e^{i\omega_d t} + \hat{a}_+^\dagger e^{-i\omega_d t}) + \epsilon_p (\hat{a}_+ e^{i\omega_p t} + \hat{a}_+^\dagger e^{-i\omega_p t}), \quad (\text{S4})$$

where ω_d (ω_p) is the pump (probe) drive frequency, ϵ_d (ϵ_p) is the strength of the signal and K_+ is the Kerr nonlinearity of polariton mode. In the frame rotating at the control drive frequency ω_d , the Hamiltonian is given by

$$H = -\Delta \hat{a}_+^\dagger \hat{a}_+ - \frac{K_+}{2} \hat{a}_+^\dagger \hat{a}_+^\dagger \hat{a}_+ \hat{a}_+ + \omega_m \hat{b}^\dagger \hat{b} + g_+ \hat{a}_+^\dagger \hat{a}_+ (\hat{b} + \hat{b}^\dagger) + \epsilon_d (\hat{a}_+ + \hat{a}_+^\dagger) + \epsilon_p (\hat{a}_+ e^{i\delta_p t} + \hat{a}_+^\dagger e^{-i\delta_p t}), \quad (\text{S5})$$

where $\Delta = \omega_d - \omega_c$, and $\delta_p = \omega_p - \omega_d$.

We ignore the quantum fluctuations and write down the equation of motion (EOM) for the mean values of the

operators. The operators $(\hat{b} + \hat{b}^\dagger)$ and $(\hat{b} - \hat{b}^\dagger)$ are essentially the normalized position and momentum, and denoted as \hat{X} and \hat{P} , respectively. The mean value $\langle \hat{O} \rangle(t)$ of any operator is represented as O from now on.

Then, the EOMs are given by

$$\dot{a}_+ = (i\Delta - \kappa/2)a_+ + iK_+ a_+^* a_+ a_+ - ig_0 a_+ X - i\epsilon_d - i\epsilon_p e^{-i\delta_p t} \quad (\text{S6a})$$

$$\dot{a}_+^* = (i\Delta - \kappa/2)a_+^* - iK_+ a_+^* a_+^* a_+ + ig_0 a_+^* X + i\epsilon_d + i\epsilon_p e^{i\delta_p t} \quad (\text{S6b})$$

$$\dot{X} = -i\omega_m P \quad (\text{S6c})$$

$$\dot{P} = -i\omega_m X - 2ig_0 a_+^* a_+ - \gamma_m P. \quad (\text{S6d})$$

To solve these equation of motions, we use a perturbative ansatz solution for weak probe. It is given by

$$a_+(t) = A_0 + A_- e^{-i\delta_p t} + A_+ e^{i\delta_p t}, \quad (\text{S7a})$$

$$X(t) = X_0 + X_- e^{-i\delta_p t} + X_+ e^{i\delta_p t}, \quad (\text{S7b})$$

$$P(t) = P_0 + P_- e^{-i\delta_p t} + P_+ e^{i\delta_p t}. \quad (\text{S7c})$$

It has a time independent static component along with two other time dependent parts. By substituting the ansatz and comparing the time independent components of Eq. S6, we arrive at the following steady state equations,

$$-i\omega_m P_0 = 0 \quad (\text{S8a})$$

$$X_0 = -\frac{2g_0|\bar{\alpha}|^2}{\omega_m} \quad (\text{S8b})$$

$$(i\Delta - \kappa/2)A_0 + iK_+A_0^*A_0^2 - ig_0A_0X_0 - i\epsilon_d = 0 \quad (\text{S8c})$$

The Eq. S8(a) essentially implies that the average momentum of the mechanical mode is zero, while Eq. S8(b) represents the static mechanical displacement denoted by X_0 . The “optical” mode’s steady state amplitude is represented by A_0 , which we will henceforth refer to as $\bar{\alpha}$. It can be computed by solving Eq. S8(c).

Our goal is to determine the response A_- at the probe frequency, which is experimentally measured quantity. In order to do this, we substitute the ansatz solutions in Eq. S6 and compare the coefficient of $e^{-i\delta_p t}$. Thus, we arrive at the following equations

[h]

$$B_1X_- = -2g_0\omega_m(\bar{\alpha}^*A_- + \bar{\alpha}A_-^*), \quad (\text{S9a})$$

$$B_2A_- = i\epsilon_p + iK_+\bar{\alpha}^2A_-^* - ig_0\bar{\alpha}X_-, \quad (\text{S9b})$$

$$B_3A_-^* = -iK_+(\bar{\alpha}^*)^2A_- + ig_0\bar{\alpha}^*X_-, \quad (\text{S9c})$$

where

$$B_1 = (\omega_m^2 - \delta_p^2 - i\gamma_m\delta_p),$$

$$B_2 = (\kappa/2 - i(\delta_p + \Delta) - 2iK_+|\bar{\alpha}|^2 - 2ig_0|\bar{\alpha}|^2/\omega_m)$$

and

$$B_3 = (\kappa/2 - i(\delta_p - \Delta) + 2iK_+|\bar{\alpha}|^2 + 2ig_0|\bar{\alpha}|^2/\omega_m).$$

Substituting the solution of X_- from Eq. S9(a) into Eq. S9(c) will results in

$$(B_3 + i|\bar{\alpha}|^2B_1')A_-^* = -i(\bar{\alpha}^*)^2(K_+ + B_1')A_-, \quad (\text{S10})$$

where $B_1' = 2g_0^2\omega_m/B_1$. Next, we substitute the solution of X and A_-^* into Eq. S9(b), and arrive at the following equation

$$\left(B_2 - i|\bar{\alpha}|^2B_1' - |\bar{\alpha}|^4 \frac{(K_+ + B_1')^2}{B_3 + i|\bar{\alpha}|^2B_1'} \right) A_- = -i\epsilon_p. \quad (\text{S11})$$

If the pump is applied at a red-detuned frequency, i.e., $\omega_d = \omega_c - \omega_m$, and the probe is near the resonator frequency, i.e., $\omega_p = \omega_c + \delta$ where $\delta = \delta_p - \omega_m$, then the component of the intracavity field A_- at frequency ω_p takes the following analytical form:

$$A_-(\delta) \approx \frac{i\epsilon_p}{-\kappa/2 + 2iK_+|\bar{\alpha}|^2 + 2ig_0|\bar{\alpha}|^2/\omega_m + i\delta - 2|\bar{\alpha}|^2g_0^2/(\gamma_m - 2i\delta) + |\bar{\alpha}|^4 \frac{(K_+ + 2ig_0^2/(\gamma_m - 2i\delta))^2}{2iK_+|\bar{\alpha}|^2 + \kappa/2 - 2i\omega_m + 2|\bar{\alpha}|^2g_0^2/\omega_m(i - \omega_m/(\gamma_m - 2i\delta))}}. \quad (\text{S12})$$

The experimentally measured cavity transmission is given by $\sqrt{\kappa_e}A_-/a_{in}$, where κ_e and a_{in} are the output coupling rate and input probe strength, respectively. The expression of A_- is obtained without the approximation of resolved sideband regime ($\omega_m \gg \kappa$). Thus, it can be used to fit the experimental data of Fig.2(c) of the main text to obtain electromechanical coupling rate g_+ .

2. In strong anharmonicity limit

When transmon qubit is detuned away from the cavity frequency, its anharmonicity is not diluted by the linear cavity and is large compared to the dissipation rate. Then, the “transmon-like” mode can still be treated as an effective two-level system (TLS) or qubit. The frequency of the TLS is given by $\tilde{\omega}_q = \omega_q + J^2/\Delta_q$, where ω_q , J and $\Delta_q = \omega_q - \omega_c$ are the bare qubit frequency, transmon-cavity coupling rate, and detuning between transmon and cavity, respectively. The shift in frequency arises from the interaction with the cavity. Thus, the system can be described as a two-level system is longitudinally coupled

to a mechanical resonator.

In the presence of a pump and a probe signal with frequency ω_d and ω_p , the Hamiltonian of the system can be written as,

$$H = \frac{\tilde{\omega}_q}{2}\hat{\sigma}^z + \omega_m\hat{b}^\dagger\hat{b} + \frac{g_0}{2}(\hat{\sigma}^z + 1)(\hat{b}^\dagger + \hat{b}) + \epsilon_d(\hat{\sigma}^+e^{-i\omega_d t} + \hat{\sigma}^-e^{i\omega_d t}) + \epsilon_p(\hat{\sigma}^+e^{-i\omega_p t} + \hat{\sigma}^-e^{i\omega_p t}) \quad (\text{S13})$$

where the $\hat{\sigma}$ ’s are the Pauli operators corresponding to the TLS and $\hat{b}(\hat{b}^\dagger)$ is the ladder operator of the mechanical mode. By shifting to a frame rotating at pump signal’s frequency ω_d , we obtain

$$H = -\frac{\Delta}{2}\hat{\sigma}^z + \omega_m\hat{b}^\dagger\hat{b} + \frac{g_0}{2}(\hat{\sigma}^z + 1)(\hat{b}^\dagger + \hat{b}) + \epsilon_d(\hat{\sigma}^+ + \hat{\sigma}^-) + \epsilon_p(\hat{\sigma}^+e^{-i\delta_p t} + \hat{\sigma}^-e^{i\delta_p t}), \quad (\text{S14})$$

where $\Delta = \omega_d - \tilde{\omega}_q$ and $\delta_p = \omega_p - \omega_d$. The Pauli operators follow the commutation relation, $[\hat{\sigma}^+, \hat{\sigma}^-] = \hat{\sigma}^z$, $[\hat{\sigma}^+, \hat{\sigma}^z] = -2\hat{\sigma}^+$, and $[\hat{\sigma}^-, \hat{\sigma}^z] = 2\hat{\sigma}^-$.

In this study, we deal with the mean response of the system and ignore the quantum fluctuation. For simplicity, the mean value $\langle \hat{O} \rangle$ of an operator is represented as O . We can construct the mean value equation using the Hamiltonian of Eq. S14 and it is given by

$$\dot{X} = -i\omega_m P, \quad (\text{S15a})$$

$$\dot{P} = -i\omega_m X - ig_0(\sigma^z + 1) - \gamma_m P, \quad (\text{S15b})$$

$$\begin{aligned} \dot{\sigma}^+ = & (-i\Delta - \gamma_q/2)\sigma^+ + ig_0 X \sigma^+ - i\epsilon_d \sigma^z \\ & - i\epsilon_p e^{i\delta_p t} \sigma^z, \end{aligned} \quad (\text{S15c})$$

$$\begin{aligned} \dot{\sigma}^- = & (i\Delta - \gamma_q/2)\sigma^- - ig_0 X \sigma^- + i\epsilon_d \sigma^z \\ & + i\epsilon_p e^{-i\delta_p t} \sigma^z, \end{aligned} \quad (\text{S15d})$$

$$\begin{aligned} \dot{\sigma}^z = & -\gamma_q(\sigma^z + 1) - 2i\epsilon_d \sigma^+ + 2i\epsilon_d \sigma^- \\ & - 2i\epsilon_p e^{-i\delta_p t} \sigma^+ + 2i\epsilon_p e^{i\delta_p t} \sigma^-. \end{aligned} \quad (\text{S15e})$$

Here, γ_q and γ_m represents the dissipation rates of the qubit and mechanical resonator respectively.

For a low enough strength of probe signal, we do a perturbative expansion of the mean values and use the Ansatz solution

$$O(t) = O_0 + O_- e^{-i\delta_p t} + O_+ e^{i\delta_p t}, \quad (\text{S16})$$

where $O(t)$ represents the mean values of the operators. The time-independent component are the steady state amplitude, whereas the coefficient of $e^{-i\delta_p t}$ represents the response at probe frequency. By substituting the ansatz solution in Eq. S15, and we arrive at the steady state equations

$$-i\omega_m P_0 = 0, \quad (\text{S17a})$$

$$-i\omega_m X_0 - ig_0(\sigma_0^z + 1) - \gamma_m P_0 = 0, \quad (\text{S17b})$$

$$(-i\Delta - \gamma_q/2)\sigma_0^+ + ig_0 X_0 \sigma_0^+ - i\epsilon_d \sigma_0^z = 0, \quad (\text{S17c})$$

$$(i\Delta - \gamma_q/2)\sigma_0^- - ig_0 X_0 \sigma_0^- + i\epsilon_d \sigma_0^z = 0, \quad (\text{S17d})$$

$$-\gamma_q(\sigma_0^z + 1) - 2i\epsilon_d \sigma_0^+ + 2i\epsilon_d \sigma_0^- = 0. \quad (\text{S17e})$$

From the above equation, we compute the steady state amplitudes

$$P_0 = 0, \quad (\text{S18a})$$

$$\sigma_0^z = -\frac{\tilde{\Delta}^2 + \gamma_q^2/4}{\tilde{\Delta}^2 + \gamma_q^2/4 + 2\epsilon_d^2}, \quad (\text{S18b})$$

$$\sigma_0^+ = i\epsilon_d \frac{\gamma_q/2 - i\tilde{\Delta}}{\tilde{\Delta}^2 + \gamma_q^2/4 + 2\epsilon_d^2}, \quad (\text{S18c})$$

$$\sigma_0^- = -i\epsilon_d \frac{\gamma_q/2 + i\tilde{\Delta}}{\tilde{\Delta}^2 + \gamma_q^2/4 + 2\epsilon_d^2}, \quad (\text{S18d})$$

$$\begin{aligned} X_0 = & -\frac{g_0}{\omega_m}(\sigma^z + 1/2) \\ = & -2 \frac{2g_0\epsilon_d^2}{\omega_m(\tilde{\Delta}^2 + \gamma_q^2/4 + 2\epsilon_d^2)}. \end{aligned} \quad (\text{S18e})$$

Here we define $\tilde{\Delta} = \Delta - g_0 X_0$.

Next, we compute the first-order coefficients, in particular σ_- , the quantity that is measured experimentally. In order to compute this, we compare the coefficients of $e^{-i\delta_p t}$ from Eq. S15(a) and (b), and substitute the steady-state amplitudes from Eq. S18. Thus, we arrive at the following equations

$$-i\omega_m P_- = -i\delta_p X_- \quad (\text{S19a})$$

$$-i\delta_p P_- = -i\omega_m X_- - ig_0 \sigma_-^z - \gamma_m P_- \quad (\text{S19b})$$

$$\begin{aligned} -i\delta_p \sigma_-^+ = & (-i\Delta - \gamma_q/2)\sigma_-^+ + ig_0 X_0 \sigma_-^+ \\ & + ig_0 X_- \sigma_0^+ - i\epsilon_d \sigma_-^z \end{aligned} \quad (\text{S19c})$$

$$\begin{aligned} -i\delta_p \sigma_-^- = & (i\Delta - \gamma_q/2)\sigma_-^- - ig_0 X_0 \sigma_-^- \\ & - ig_0 X_- \sigma_0^- + i\epsilon_d \sigma_-^z + i\epsilon_p \sigma_0^z \end{aligned} \quad (\text{S19d})$$

$$-i\delta_p \sigma_-^z = -\gamma_q \sigma_-^z - 2i\epsilon_d(\sigma_-^+ - \sigma_-^-) - 2i\epsilon_p \sigma_0^z \quad (\text{S19e})$$

From Eq. S19(a) and (b) we get

$$X_- = B_4 \sigma_-^z, \quad (\text{S20})$$

where

$$B_4 = -\frac{ig_0}{i\omega_m + (\gamma_m - i\delta_p) \frac{\delta_p}{\omega_m}}.$$

From Eq. S19(c) and (e) and using the solution of X_- form Eq. S20, we arrive at

$$\sigma_-^+ = B_5 \sigma_-^z, \quad (\text{S21a})$$

$$\sigma_-^z = B_6 \sigma_-^- + B_7. \quad (\text{S21b})$$

Here,

$$B_5 = \frac{i\epsilon_d - B_4\epsilon_d g_0(\gamma_q/2 - i\tilde{\Delta})/(\tilde{\Delta}^2 + \gamma_q^2/4 + 2\epsilon_d^2)}{\gamma_q/2 - i(\delta_p - \tilde{\Delta})},$$

$$B_6 = \frac{2i\epsilon_d}{\gamma_q - i\delta_p + 2i\epsilon_d B_5},$$

and

$$B_7 = \frac{2\epsilon_p\epsilon_d}{(\gamma_q - i\delta_p + 2i\epsilon_d B_5)} \frac{(\gamma_q/2 - i\tilde{\Delta})}{(\tilde{\Delta}^2 + \gamma_q^2/4 + 2\epsilon_d^2)}$$

Finally, from Eq. S19(c) we compute the analytical expression of σ_- . It is given by

$$B_8\sigma_- = \left(i\epsilon_d - \frac{g_0\epsilon_d B_4(\gamma_q/2 + i\tilde{\Delta})}{\tilde{\Delta}^2 + \gamma_q^2/4 + 2\epsilon_d^2} \right) B_7 - i\epsilon_p, \quad (\text{S22})$$

where

$$B_8 = \gamma_q/2 - i(\tilde{\Delta} + \delta_p) - \left(i\epsilon_d - \frac{g_0\epsilon_d B_4(\gamma_q/2 + i\tilde{\Delta})}{\tilde{\Delta}^2 + \gamma_q^2/4 + 2\epsilon_d^2} \right) B_6. \quad (\text{S23})$$

Here, σ_0^z has been approximated to be -1 , assuming the pump strength ϵ_d to be comparatively low than decay rates. Additionally, in the experimental setup of Device-2, it holds that g_0 and ϵ_d are much smaller than γ_q . Consequently, we can approximate $\tilde{\Delta} \approx \Delta$. For a red detuned pump signal, i.e. $\Delta = \omega_d - \tilde{\omega}_q = \omega_m$, the expression of σ_- can be computed from Eq. S22. This expression (with a normalization factor) is used to fit the data points in Fig.2(e) of the main text, resulting in the solid black curve.

SUPPLEMENTARY NOTE 4.

A. Backaction from a weakly nonlinear-Kerr mode

In this section, we analyze the backaction exerted on the mechanical resonator arising due to the optomechanical interaction of the polariton modes. Because of large spectral separation, we solely focus on the upper polariton mode, leading to a simplified two-mode analysis. Considering the upper polariton mode as a weak-Kerr oscillator, in a frame rotating at the pump frequency, the Hamiltonian of the system can be expressed as

$$\mathcal{H} = -\Delta\hat{a}_+^\dagger\hat{a}_+ - \frac{K_+}{2}\hat{a}_+^\dagger\hat{a}_+^\dagger\hat{a}_+\hat{a}_+ + \omega_m\hat{b}^\dagger\hat{b} + g_+\hat{a}_+^\dagger\hat{a}_+(\hat{b} + \hat{b}^\dagger) + \epsilon(\hat{a}_+ + \hat{a}_+^\dagger), \quad (\text{S24})$$

where K_+ is the Kerr-nonlinearity of the upper polariton mode, ϵ is the drive strength of the pump, $\Delta = \omega_d - \omega_+$

is the drive detuning, and the rest of the symbols have their usual meaning.

The quantum Langevin equations of the system are given by

$$\dot{\hat{a}}_+ = -i[\hat{a}_+, \mathcal{H}] - \frac{\kappa}{2}\hat{a}_+ + \sqrt{\kappa_{ex}}\hat{a}_{in} + \sqrt{\kappa_0}\hat{f}_{in}, \quad (\text{S25a})$$

$$\dot{\hat{b}} = -i[\hat{b}, \mathcal{H}] - \frac{\gamma}{2}\hat{b} + \sqrt{\gamma_m}\hat{b}_{in}, \quad (\text{S25b})$$

where \hat{a}_{in} , \hat{f}_{in} are noise operators of the polariton mode and \hat{b}_{in} is noise operator of the mechanical mode, $\kappa(\gamma_m)$ is the decay rate of the polariton (mechanical) mode, and $\kappa_{ex}(\kappa_0)$ are the total external(internal) decay rates of the polariton mode, respectively. Using the Hamiltonian in Eq. S24 and Eq. S25, we obtain the equations of motion (EOM) of both modes:

$$\begin{aligned} \dot{\hat{a}}_+ &= (i\Delta - \frac{\kappa}{2})\hat{a}_+ + iK_+\hat{a}_+^\dagger\hat{a}_+\hat{a}_+ - ig_0\hat{a}_+(\hat{b} + \hat{b}^\dagger) \\ &\quad + \epsilon + \sqrt{\kappa_{ex}}\hat{a}_{in} + \sqrt{\kappa_0}\hat{f}_{in}, \end{aligned} \quad (\text{S26a})$$

$$\dot{\hat{b}} = (-i\omega_m - \frac{\gamma_m}{2})\hat{b} - ig_0\hat{a}_+^\dagger\hat{a}_+ + \sqrt{\gamma_m}\hat{b}_{in}. \quad (\text{S26b})$$

By defining the mean field occupation of the polariton mode and the mechanical mode as α and β , respectively, we arrive at the following semi-classical equations of motion:

$$\dot{\alpha} = (i\Delta - \frac{\kappa}{2})\alpha + iK_+|\alpha|^2\alpha - ig_0\alpha(\beta + \beta^*) + \epsilon, \quad (\text{S27a})$$

$$\dot{\beta} = (-i\omega_m - \frac{\gamma_m}{2})\beta - ig_0|\alpha|^2. \quad (\text{S27b})$$

In the steady state of the system, these equations become $\dot{\alpha} = 0$, $\dot{\beta} = 0$. Solving these, we find the steady state field amplitude $\bar{\alpha}$ and $\bar{\beta}$.

Next, we assume an ansatz solution of Eq. S26, where we write down the fields as a combination of steady state amplitude and a fluctuation term, i.e. $\hat{a}_+ = \bar{\alpha} + \delta\hat{a}_+$, and $\hat{b} = \bar{\beta} + \delta\hat{b}$. Substituting these ansatz to Eq. S26, and ignoring the higher order fluctuation terms, we get the EOMs as,

$$\begin{aligned} \delta\dot{\hat{a}}_+ &= \left[i\tilde{\Delta} - \frac{\kappa}{2} \right] \delta\hat{a}_+ + i\eta\delta\hat{a}_+^\dagger - iG(\delta\hat{b} + \delta\hat{b}^\dagger) + \sqrt{\kappa_{ex}}\hat{a}_{in} \\ &\quad + \sqrt{\kappa_0}\hat{f}_{in}, \end{aligned} \quad (\text{S28a})$$

$$\begin{aligned} \delta\dot{\hat{a}}_+^\dagger &= \left[-i\tilde{\Delta} - \frac{\kappa}{2} \right] \delta\hat{a}_+^\dagger - i\eta^*\delta\hat{a}_+ + iG^*(\delta\hat{b} + \delta\hat{b}^\dagger) + \\ &\quad \sqrt{\kappa_{ex}}\hat{a}_{in}^\dagger + \sqrt{\kappa_0}\hat{f}_{in}^\dagger, \end{aligned} \quad (\text{S28b})$$

$$\dot{\delta\hat{b}} = \left[-i\omega_m - \frac{\gamma_m}{2}\right] \delta\hat{b} - iG^* \delta\hat{a}_+ - iG \delta\hat{a}_+^\dagger + \sqrt{\gamma_m} \hat{b}_{in}, \quad (\text{S28c})$$

$$\dot{\delta\hat{b}}^\dagger = \left[i\omega_m - \frac{\gamma_m}{2}\right] \delta\hat{b}^\dagger + iG \delta\hat{a}_+^\dagger + iG^* \delta\hat{a}_+ + \sqrt{\gamma_m} \hat{b}_{in}^\dagger, \quad (\text{S28d})$$

where $\tilde{\Delta} = \Delta + 2K_+ |\bar{\alpha}|^2 - g_0(\bar{\beta} + \bar{\beta}^*)$, $G = g_0 \bar{\alpha}$ and $\eta = K_+ \bar{\alpha}^2$.

Next, we perform Fourier transform of the above equations by defining the transformation as $x[\omega] = \mathcal{F}[x(t)] = \int_{-\infty}^{+\infty} x(t) e^{i\omega t} dt$. Using the identities $(x^\dagger)[\omega] = (x[-\omega])^\dagger$, and $\mathcal{F}[\dot{x}(t)] = -i\omega \mathcal{F}[x(t)]$, the new set of equations of motion in frequency domain become,

$$\begin{bmatrix} \chi_c^{-1} & -i\eta \\ i\eta^* & \tilde{\chi}_c^{-1} \end{bmatrix} \begin{bmatrix} \delta\hat{a}_+[\omega] \\ (\delta\hat{a}_+^\dagger)[\omega] \end{bmatrix} = -i \begin{bmatrix} G & G \\ -G^* & -G^* \end{bmatrix} \begin{bmatrix} \delta\hat{b}[\omega] \\ (\delta\hat{b}^\dagger)[\omega] \end{bmatrix} + \begin{bmatrix} \sqrt{\kappa_{ex}} \hat{a}_{in}[\omega] + \sqrt{\kappa_0} \hat{f}_{in}[\omega] \\ \sqrt{\kappa_{ex}} (\hat{a}_{in}^\dagger)[\omega] + \sqrt{\kappa_0} (\hat{f}_{in}^\dagger)[\omega] \end{bmatrix} \quad (\text{S29})$$

$$\begin{bmatrix} \chi_m^{-1} & 0 \\ 0 & \tilde{\chi}_m^{-1} \end{bmatrix} \begin{bmatrix} \delta\hat{b}[\omega] \\ (\delta\hat{b}^\dagger)[\omega] \end{bmatrix} = -i \begin{bmatrix} G^* & G \\ -G^* & -G \end{bmatrix} \begin{bmatrix} \delta\hat{a}_+[\omega] \\ (\delta\hat{a}_+^\dagger)[\omega] \end{bmatrix} + \begin{bmatrix} \sqrt{\gamma_m} \hat{b}_{in}[\omega] \\ \sqrt{\gamma_m} (\hat{b}_{in}^\dagger)[\omega] \end{bmatrix}, \quad (\text{S30})$$

where $\chi_c^{-1}[\omega] = (-i(\omega + \tilde{\Delta}) + \kappa/2)$, $\tilde{\chi}_c^{-1}[\omega] = (-i(\omega - \tilde{\Delta}) + \kappa/2)$ are dressed mode's susceptibilities and $\chi_m^{-1}[\omega] = (-i(\omega - \omega_m) + \gamma_m/2)$, $\tilde{\chi}_m^{-1}[\omega] = (-i(\omega + \omega_m) + \gamma_m/2)$ is the mechanical susceptibilities.

To find the effective dynamics of the mechanical res-

onator, we first solve Eq. S29, and substitute the solution of $(\delta\hat{a}_+)[\omega]$ and $(\delta\hat{a}_+^\dagger)[\omega]$ in Eq. S30. This leads to the simplified equations of the mechanical mode as,

$$\begin{bmatrix} -i(\omega - \omega_m) + \frac{\gamma_m}{2} + \Sigma_c[\omega] & \Sigma_c[\omega] \\ -\Sigma_c[\omega] & -i(\omega + \omega_m) + \frac{\gamma_m}{2} - \Sigma_c[\omega] \end{bmatrix} \begin{bmatrix} \delta\hat{b}[\omega] \\ (\delta\hat{b}^\dagger)[\omega] \end{bmatrix} = \sqrt{\gamma_m} \begin{bmatrix} \hat{B}_{in}[\omega] \\ (\hat{B}_{in}^\dagger)[\omega] \end{bmatrix}. \quad (\text{S31})$$

The quantity defined as $\Sigma_c[\omega] = 2i|G|^2[\tilde{\Delta} - |\eta|[1/\chi_c \tilde{\chi}_c - |\eta|^2]^{-1}]$ represents the modification in the mechanical resonator's dynamics due to nonlinear Kerr mode. The frequency shift and the effective optomechanical damping rate of the mechanical resonator is given by, $\delta\omega_m = \text{Im}(\Sigma_c[\omega_m])$ and $\Gamma_m = \gamma_m + 2 \times \text{Re}(\Sigma_c[\omega_m])$, respectively. These two quantities are plotted for Device-2 parameters in Fig. S4 as a function of pump strength and detuning. It illustrates how the backaction effect evolves as parameters change.

In Fig. 3(a) of the main text, we plot Γ_m and $\delta\gamma_m$ as solid black lines using Device-1's parameters. Similarly, by using the parameters of Device-2, the boundary of mechanical instability is derived from the threshold $\text{Re}(\Sigma_c[\omega]) = -\gamma_m/2$ and it is plotted as the solid black line in Fig. 3(c) of the main text. The same is shown in Fig. S4 as the gray curve. By replacing $K_+ = 0$ in the expression of $\Sigma_c[\omega_m]$, we can calculate the boundary of mechanical instability for a linear resonator coupled to the mechanical resonator. It is shown as the dashed curve in Fig. 3(c) of the main text.

SUPPLEMENTARY NOTE 5.

Linear stability test using semi-classical analysis of three-mode system

We start with the Hamiltonian of the three-mode system consisting of a linear cavity, transmon qubit, and a mechanical resonator. In the presence of a drive signal, it can be written as

$$H = \omega_c a^\dagger a + \omega_q c^\dagger c - \frac{\alpha_T}{2} c^\dagger c^\dagger c c + J(ac^\dagger + a^\dagger c) + \omega_m b^\dagger b + g_0 c^\dagger c(b + b^\dagger) + \epsilon(ae^{i\omega_d t} + a^\dagger e^{-i\omega_d t}), \quad (\text{S32})$$

where J is the coupling strength between cavity and transmon, g_0 is the electromechanical coupling between the transmon and the mechanical resonator, α_T is the transmon anharmonicity, $a(a^\dagger)$, $c(c^\dagger)$ and $b(b^\dagger)$ are the annihilation(creation) operators of cavity, transmon, and mechanical modes with resonant frequencies of ω_c , ω_q and ω_m , respectively. A pump signal is continuously applied to the cavity with strength ϵ and frequency ω_d . In the rotating frame of pump frequency, the Hamiltonian be-

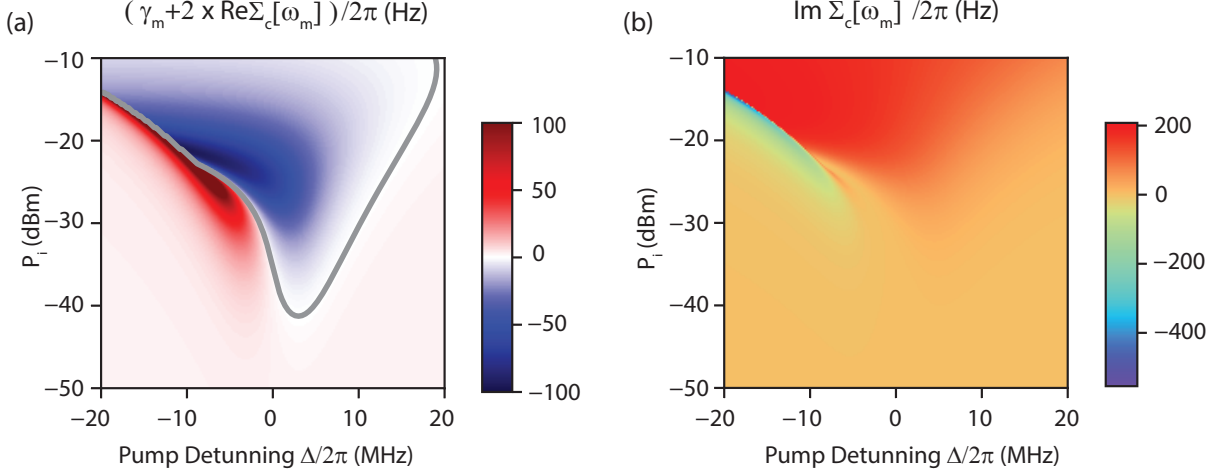


FIG. S4. **Backaction from weak Kerr oscillator model:** Colorplot in (a) and (b) shows the effective mechanical linewidth $\Gamma_m = \gamma_m + 2 \times \text{Re}(\Sigma_c[\omega_m])$ and optomechanical frequency shift $\delta\omega_m = \text{Im}(\Sigma_c[\omega_m])$, respectively. To maintain the visibility of small variations, the color scale in (a) is truncated at ± 100 Hz. The gray curve in (a) denotes the contour of $\Gamma_m = 0$. These quantities are computed from a model where the EM mode is considered as an anharmonic oscillator, and it is longitudinally coupled to the mechanical resonator. The parameters used to compute these quantities are taken from device-2, and they are given by $\gamma_m/2\pi \sim 6$ Hz, $\omega_m/2\pi \sim 3.97$ kHz, $K_+/2\pi \sim 8.55$ MHz, $\kappa/2\pi \sim 9$ MHz and $g_+/2\pi \sim 45$ kHz.

comes

$$H = -\Delta_1 a^\dagger a - \Delta_2 c^\dagger c - \frac{\alpha_c}{2} c^\dagger c^\dagger c c + J(a c^\dagger + a^\dagger c) + \omega_m b^\dagger b + g_0 c^\dagger c(b + b^\dagger) + \epsilon(a + a^\dagger), \quad (\text{S33})$$

where $\Delta_1 = (\omega_d - \omega_c)$ and $\Delta_2 = (\omega_d - \omega_q)$.

Writing the Heisenberg-Langevin equations and using semi-classical approximation, we get the steady state equation of motions as

$$\dot{\alpha}' = -(\kappa_b/2 - i\Delta_1)\alpha' - iJ\zeta - i\epsilon, \quad (\text{S34a})$$

$$\dot{\zeta} = -[\gamma/2 - i\Delta_2 - 2i\alpha_T|\zeta|^2 + ig_0\zeta(\beta + \beta^*)] - iJ\alpha', \quad (\text{S34b})$$

$$\dot{\beta} = -(-\gamma_m/2 + i\omega_m)\beta - ig_0|\zeta|^2, \quad (\text{S34c})$$

where $\langle a \rangle = \alpha'$, $\langle c \rangle = \zeta$ and $\langle b \rangle = \beta$ are the mean values.

Subsequently, representing the steady-state amplitudes in complex form as $\alpha' = x + iy$, $\zeta = p + iq$, and $\beta = u + iv$, we get the following sets of equations

$$\dot{x} = \dot{f}_1 = -\frac{\kappa_b}{2}x - \Delta_1 y + Jq \quad (\text{S35a})$$

$$\dot{y} = \dot{f}_2 = +\Delta_1 x - \frac{\kappa_b}{2}y - Jp - \epsilon \quad (\text{S35b})$$

$$\dot{p} = \dot{f}_3 = -\frac{\gamma}{2}p + (-\Delta_2 - 2\alpha_T(p^2 + q^2) + 2g_0u)q + Jy \quad (\text{S35c})$$

$$\dot{q} = \dot{f}_4 = -\frac{\gamma}{2}q - (-\Delta_2 - 2\alpha_T(p^2 + q^2) + 2g_0u)p - Jx \quad (\text{S35d})$$

$$\dot{u} = \dot{f}_5 = -\frac{\gamma_m}{2}u + \omega_m v \quad (\text{S35e})$$

$$\dot{v} = \dot{f}_6 = -\omega_m u - \frac{\gamma_m}{2}v - g_0(p^2 + q^2) \quad (\text{S35f})$$

For the steady-state solution or the fix point of the system, we set the first derivatives to zero i.e., $\dot{x} = \dot{y} = \dot{p} = \dot{q} = \dot{u} = \dot{v} = 0$. It leaves us with

$$\frac{\gamma_m^2}{4\omega_m}u + \omega_m u - g_0 \left(\frac{J\kappa_b\epsilon}{2AB}p(u) + \frac{J\Delta_1\epsilon}{AB}q(u) \right) = 0, \quad (\text{S36})$$

where

$$A = \frac{\kappa_b^2}{4} + \Delta_1^2$$

$$B = \left(\frac{\gamma}{2} + \frac{J^2\kappa_b}{2A} \right),$$

$$C = -\Delta_2 - 2\alpha_T(p^2 + q^2) + 2g_0u + \frac{J^2\Delta_1}{A}.$$

Here,

$$p(u) = -\frac{\left(\frac{J\Delta_1 C}{A} + \frac{J\kappa_b B}{2A} \right) \epsilon}{B^2 + C^2},$$

and

$$q(u) = \frac{\left(\frac{-J\Delta_1 B}{A} + \frac{J\kappa_b C}{2A}\right)\epsilon}{B^2 + C^2}.$$

By finding the roots of Eq.S36, the fixed points x, y, p, q, u and v can be obtained. Considering the steady-state values as $(\bar{x}, \bar{y}, \bar{p}, \bar{q}, \bar{u}, \bar{v})$, the nature of these points can be understood by perturbing these points and finding the time evolution of the perturbation. Defining the perturbation as $z_i = k_i - \bar{k}_i$, where k_i for $i = 1, 2, 3, 4, 5, 6$ corresponds to (x, y, p, q, u, v) , respectively. Subsequently, the time evolution of perturbation z_i is obtained as,

$$\dot{z}_i = \dot{k}_i \approx f_i|_{\bar{k}} + \sum_i (k_i - \bar{k}_i) \frac{\partial f_i}{\partial k_i}|_{\bar{k}_i}. \quad (\text{S37})$$

This gives

$$S = \begin{bmatrix} -\frac{\kappa_b}{2} & -\Delta_1 & 0 \\ \Delta_1 & -\frac{\kappa_b}{2} & -J \\ 0 & J & -\frac{\gamma}{2} - 4\alpha_T \bar{p} \bar{q} \\ -J & 0 & \Delta_2 + 6\alpha_T \bar{p}^2 + 2\alpha_T \bar{q}^2 - 2g_0 \bar{u} \\ 0 & 0 & 0 \\ 0 & 0 & -2g_0 \bar{p} \end{bmatrix}$$

The Eq. S39 has the solution of the form $z(t) = \sum_i b_i w_i e^{\lambda_i t}$, where b_i 's are the constant of integration, λ_i 's are the eigenvalues of the matrix S and w_i 's are the corresponding eigenvectors. Thus, any eigenvalue of the S with a positive real part will cause the solution for $z(t)$ to grow exponentially, resulting in instability. Thus, this becomes a criterion for identifying the unstable points.

Fig. 6(c) of the main text shows the result of such a calculation for Device-2. The parameters used for the calculation are mentioned below. A bare cavity decay rate of $\kappa_b \sim 8$ MHz and transmon dissipation rate of $\gamma \sim 12$ MHz is used for the calculation. The electromechanical coupling between the transmon and mechanical resonator is set to 300 kHz, which was estimated from the upper-polariton mode's flux responsivity, given in Fig. S3. It is evident that a semi-classical description of the system is not sufficient to understand the experimental observation of mechanical parametric instability.

$$\frac{d}{dt} \begin{bmatrix} z_1 \\ z_2 \\ z_3 \\ z_4 \\ z_5 \\ z_6 \end{bmatrix} = \begin{bmatrix} \frac{\partial f_1}{\partial x} & \frac{\partial f_1}{\partial y} & \frac{\partial f_1}{\partial p} & \frac{\partial f_1}{\partial q} & \frac{\partial f_1}{\partial u} & \frac{\partial f_1}{\partial v} \\ \frac{\partial f_2}{\partial x} & \frac{\partial f_2}{\partial y} & \frac{\partial f_2}{\partial p} & \frac{\partial f_2}{\partial q} & \frac{\partial f_2}{\partial u} & \frac{\partial f_2}{\partial v} \\ \frac{\partial f_3}{\partial x} & \frac{\partial f_3}{\partial y} & \frac{\partial f_3}{\partial p} & \frac{\partial f_3}{\partial q} & \frac{\partial f_3}{\partial u} & \frac{\partial f_3}{\partial v} \\ \frac{\partial f_4}{\partial x} & \frac{\partial f_4}{\partial y} & \frac{\partial f_4}{\partial p} & \frac{\partial f_4}{\partial q} & \frac{\partial f_4}{\partial u} & \frac{\partial f_4}{\partial v} \\ \frac{\partial f_5}{\partial x} & \frac{\partial f_5}{\partial y} & \frac{\partial f_5}{\partial p} & \frac{\partial f_5}{\partial q} & \frac{\partial f_5}{\partial u} & \frac{\partial f_5}{\partial v} \\ \frac{\partial f_6}{\partial x} & \frac{\partial f_6}{\partial y} & \frac{\partial f_6}{\partial p} & \frac{\partial f_6}{\partial q} & \frac{\partial f_6}{\partial u} & \frac{\partial f_6}{\partial v} \end{bmatrix} \begin{bmatrix} z_1 \\ z_2 \\ z_3 \\ z_4 \\ z_5 \\ z_6 \end{bmatrix}. \quad (\text{S38})$$

Upon substituting the values of f_i 's and evaluating the derivative at the steady state points, we get

$$\frac{d}{dt} \begin{bmatrix} z_1 \\ z_2 \\ z_3 \\ z_4 \\ z_5 \\ z_6 \end{bmatrix} = S \begin{bmatrix} z_1 \\ z_2 \\ z_3 \\ z_4 \\ z_5 \\ z_6 \end{bmatrix}. \quad (\text{S39})$$

The S -matrix governs the evolution of the perturbation, and it is given by

$$S = \begin{bmatrix} J & 0 & 0 \\ 0 & 0 & 0 \\ -\Delta_2 - 2\alpha_T \bar{p}^2 - 6\alpha_T \bar{q}^2 + 2g_0 \bar{u} & 2g_0 \bar{q} & 0 \\ -\frac{\gamma}{2} + 4\alpha_T \bar{p} \bar{q} & -2g_0 \bar{p} & 0 \\ 0 & -\frac{\Gamma}{2} & \omega_m \\ -2g_0 \bar{q} & -\omega_m & -\frac{\Gamma}{2} \end{bmatrix}. \quad (\text{S40})$$

SUPPLEMENTARY NOTE 6.

Modelling of the instability region using polariton basis

We find out in the previous section that a classical description of the system fails to describe the experimental observation. Therefore, a quantum mechanical description of electrical modes is necessary to explain the observations at low to moderate pump powers. This is done by treating each transition into their two-level subspace. Alternatively one can treat the electrical modes as a multi-level atom. However, such an analysis quickly becomes intractable. We justify the validity of two-level model using the fact that a pump near a certain transition frequency only drive that particular transition occurs due to the large spectral separation compared to their decay rates. In addition, these transitions are flux tunable as shown in the Fig .4(a) of the main text, resulting in coupling with the mechanical resonator. Thus, the full system can be treated as a multiple two-level systems (TLS) independently coupled to the mechanical resonator with a certain coupling strength. We separately compute the region of mechanical instability for each TLS and super-

pose them together to compute the full instability phase space diagram.

We begin the theoretical analysis by computing the frequency ω_i and electromechanical coupling strength g_i for each TLS. The transition frequencies ω_i 's are obtained from the difference of eigenenergies of the transmon-cavity system. The Hamiltonian of the transmon-cavity

$$H = \begin{bmatrix} 0 & 0 & 0 & 0 & 0 & 0 \\ 0 & \omega_q & J & 0 & 0 & 0 \\ 0 & J & \omega_c & 0 & 0 & 0 \\ 0 & 0 & 0 & 2(\omega_q - \alpha_c) & \sqrt{2}J & 0 \\ 0 & 0 & 0 & \sqrt{2}J & \omega_c + \omega_q & \sqrt{2}J \\ 0 & 0 & 0 & 0 & \sqrt{2}J & 2\omega_c \end{bmatrix} \xrightarrow{\text{Diagonalization}} \begin{bmatrix} 0 & 0 & 0 & 0 & 0 & 0 \\ 0 & E_1 & 0 & 0 & 0 & 0 \\ 0 & 0 & E_2 & 0 & 0 & 0 \\ 0 & 0 & 0 & E_3 & 0 & 0 \\ 0 & 0 & 0 & 0 & E_4 & 0 \\ 0 & 0 & 0 & 0 & 0 & E_5 \end{bmatrix}, \quad (\text{S41})$$

where E_i 's are a function of $\omega_q, \omega_c, \alpha_T$ and J . Using these energy eigenvalues, we obtain the transition frequencies ω_i 's by calculating the difference between the relevant energy eigenvalues, as shown by the arrows in Fig. S5. In terms of notation used in the main text, the frequencies $\omega_-, \omega_+, \omega_{-\alpha}$ and $\omega_{-\beta}$ correspond to $\omega_1, \omega_2, \omega_3$ and ω_4 , respectively.

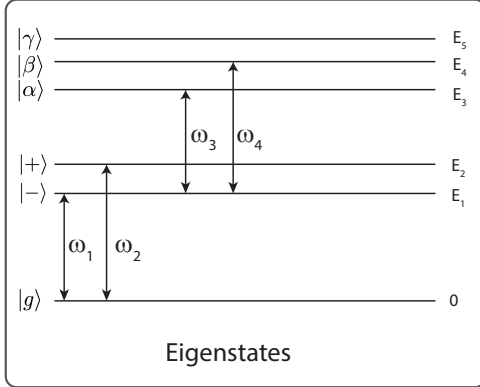


FIG. S5. **Eigenstates:** Energy eigenstates of the cavity-transmon system. The energies are indicated on the right, while the eigenstates are labeled on the left. ω_i 's represent the transition energies, and the arrows point to the appropriate eigenstates for the specific transition.

Next, we determine the electromechanical coupling strengths for each transition. In the presence of magnetic field the transmon frequency becomes a function of mechanical displacement x , i.e. $\omega_q(x) \approx \omega_q^{\text{bare}} + G_q x$. Consequently, the transition frequencies become a function of mechanical displacement as well, since they rely on ω_q . Therefore, by doing Taylor's expansion of ω_i 's up to first order in x , we get

$$\omega_i \approx \omega_i|_{x=0} + G'_i x. \quad (\text{S42})$$

Here, $G'_i = \frac{\partial \omega_i}{\partial x}|_{x=0}$ is the frequency shift per unit

system (ignoring the mechanical resonator) is given by $H = \omega_c a^\dagger a + \omega_q c^\dagger c - \frac{\alpha_T}{2} c^\dagger c^\dagger c c + J(a c^\dagger + a^\dagger c)$, where \hat{a} and \hat{c} are the ladder operators of cavity and transmon, respectively. We write the Hamiltonian up to two-excitation subspace and subsequently diagonalize it to find the energy eigenvalues. It is given by

displacement. Thus, the electromechanical coupling strength for i 'th transition is then given by

$$g_i = \frac{\partial \omega_i}{\partial x} x_{zpf} = \frac{\partial \omega_i}{\partial \Phi} \frac{\partial \Phi}{\partial x} x_{zpf} = G_i B^\parallel l x_{zpf}, \quad (\text{S43})$$

where $G_i = d\omega_i/d\Phi$ is the flux responsivity. Since G_i 's are a function of ω_q , we can estimate the remainder by computing the value of any one of the G_i . Here, G_2 is essentially the flux responsivity of the upper polariton mode, and it is measured experimentally, as shown in Fig. S3. From this known value of G_2 we calculate the remaining G_i 's and hence the coupling strength g_i .

The Hamiltonian of any specific two-level system takes the form (in the interaction picture)

$$H = -\Delta_i \frac{\sigma_i^z}{2} + \omega_m b^\dagger b + \frac{g_i}{2} (\sigma_i^z + 1)(b + b^\dagger) + \epsilon_i (\sigma_i^+ + \sigma_i^-), \quad (\text{S44})$$

where $\Delta_i = (\omega_d - \omega_i)$, ω_d is the drive frequency and ω_i is the frequency of the i 'th transitions, g_i is the single photon electromechanical coupling, and ϵ_i is the drive amplitude.

In order to find the phase diagram of unstable response of the mechanical resonator, we follow the same approach as described in the previous section. It starts with writing the Heisenberg-Langevin equation for σ 's and b , followed by deriving the steady state equation of motion of the mean values of the operators:

$$\dot{\sigma}_i^z = -i(2\epsilon\sigma^+ - 2\epsilon\sigma^-) - \gamma_i(\sigma_i^z + 1) \quad (\text{S45a})$$

$$\dot{\sigma}_i^- = -i(-\Delta_i \sigma_i^- + G_i x \sigma_i^- - \epsilon \sigma_i^z) - \left(\frac{\gamma_i}{2} + \gamma_i^\phi\right) \sigma_i^- \quad (\text{S45b})$$

$$\dot{\sigma}_i^+ = i(-\Delta_i \sigma_i^+ + G_i x \sigma_i^+ - \epsilon \sigma_i^z) - \left(\frac{\gamma_i}{2} + \gamma_i^\phi\right) \sigma_i^+ \quad (\text{S45c})$$

$$\dot{b} = -i\frac{g_i}{2}(\sigma_i^z + 1) + \omega_m b - \frac{\gamma_m}{2} b \quad (\text{S45d})$$

Here we use the notations σ and b in place of $\langle\sigma\rangle$ and $\langle b\rangle$ to represent the mean values. γ_i and γ_ϕ are the energy dissipation rate and the dephasing rate of the i 'th transition. We write the mean values in complex form as $\sigma^z = s$, $\sigma^+ = p' + iq'$, and $b = u + iv$.

It is followed by the calculation of fixed points, which is carried out by setting the first time derivative of the mean values to zero. It leaves us with

$$\left(\frac{\gamma_i}{2} + \gamma_i^\phi\right) q'(s) = -\Delta_i p'(s) + 2g_i u(s) p'(s) - \epsilon s, \quad (\text{S46})$$

where

$$\begin{aligned} q'(s) &= \frac{\gamma_i}{4\epsilon}(s+1), \\ u(s) &= -\frac{\frac{g}{2}(s+1)}{\frac{\gamma_m^2}{4\omega_m} + \omega_m}, \\ v(s) &= -\frac{\frac{g\gamma_m}{4\omega_m}(s+1)}{\frac{\gamma_m^2}{4\omega_m} + \omega_m}, \end{aligned}$$

and

$$p'(s) = -q'(s) \frac{-\Delta_i + 2gu(s)}{\gamma_i/2 + \gamma_i^\phi}.$$

Subsequently, we determine the nature of these fixed points by finding the time evolution of a small perturbation. Following the same approach given in the previous section, we compute the evolution matrix of the perturbation. It is given by,

$$S = \begin{bmatrix} -\gamma_i & 0 & 4\epsilon_i & 0 & 0 \\ 0 & -(\gamma_i/2 + \gamma_i^\phi) & \Delta_i - 2gu & -2gq' & 0 \\ -\epsilon & \Delta + 2gu & -(\gamma_i/2 + \gamma_i^\phi) & 2gp' & 0 \\ 0 & 0 & 0 & \frac{-\gamma_m}{2} & \omega_m \\ \frac{-g}{2} & 0 & 0 & -\omega_m & \frac{-\gamma_m}{2} \end{bmatrix} \quad (\text{S47})$$

If the real part of the eigenvalue becomes positive for a certain value of Δ and ϵ , we denote that point in the phase space as unstable. Hence, we compute the mechanical instability phase diagram of the four relevant two-level systems with frequencies $\omega_1, \omega_2, \omega_3$ and ω_4 , respectively. Subsequently, we plot all four regions together, resulting in the green shaded area in Fig. 6(b) of the main text.

It is evident from the transmission spectrum of Fig. 4(b) in the main text that the linewidths associated with each transition are not equal. The higher-level transitions have larger linewidth compared to the lower-level transitions. The energy decay rates and dephasing rates used to compute Fig. 6(b) of the main text are given by $\gamma_1 \sim 10$ MHz, $\gamma_1^\phi \sim 4$ MHz, $\gamma_2 \sim 10$ MHz,

$\gamma_2^\phi \sim 4$ MHz, $\gamma_3 \sim 18$ MHz, $\gamma_3^\phi \sim 8$ MHz, $\gamma_4 \sim 14$ MHz, and $\gamma_4^\phi \sim 9$ MHz. The onset of instability for each transition depends on these decay rates, as observed in the Fig 6(b) of the main text.

In addition, the onset of instability depends on the thermal occupation of the eigenstates. The ground and excited state occupation of a certain TLS determines the probability of transition when subjected to a drive. Since $|+\rangle$ and $|-\rangle$ have much smaller thermal occupations than $|g\rangle$, the higher transitions with frequencies of ω_3 and ω_4 are less likely to occur than lower transitions with frequencies of ω_1 and ω_2 . While computing the instability boundary, we consider 82% thermal occupation in $|g\rangle$ while 10% and 8% occupation in $|-\rangle$ and $|+\rangle$, respectively. These values were inspired from the numerical calculation of Fig. 5(b) in the main text, which resulted in a good match with the experiment. The eigenstates $|\alpha\rangle$, $|\beta\rangle$ and $|\gamma\rangle$ are considered to have zero thermal occupation due to the high value of their energy.

A. Data recording procedure for instability measurements

We describe the details of the data gathering routine for CEQA and power spectral density (PSD) measurements. For the CEQA experiment, we use a vector network analyser(VNA) to measure the probe transmission, whereas a separate signal generator supplies the pump signal. Both microwave units are synchronized using the 10 MHz reference signal. Since we use very low probe powers, we record three traces of the transmissions, which are later averaged to reduce the trace noise. The measurements are taken at a bandwidth of 10 Hz to improve the signal-to-noise.

For the instability measurements, we record the power spectral density (PSD) of the outgoing microwave signal using a signal analyzer. For Fig. 3(a) of the main text, the PSD is recorded at a resolution bandwidth(RBW) of 3 Hz and with 200 averages, which takes 2 minutes to acquire each data point. The PSD is recorded around mechanical sideband frequency $\omega_d + \omega_m$ with 1 kHz span, where ω_d is the pump frequency.

For the data corresponding to mechanical instability in Fig. 3(b) of main text, the PSD is recorded in a span of 30 MHz with center frequency ω_d . The spectrum analyzer RBW is set to 5 kHz and average to 1000, which take nearly 20 s for a single realization of pump power and detuning. For the phase diagram of instability in Fig. 5(a) and (c) of the main text, we record the PSD neighboring two mechanical sidebands $\omega_d \pm 2\omega_m$ successively, with a span of 2 kHz. An unstable mechanical resonator will cause a large amplitude in the PSD around $\omega_d \pm 2\omega_m$. Thus, it is sufficient to record the data in these two region to conclude about the mechanical instability. We set the spectrum analyzer's RBW to 5 Hz and average to 10. It reduces the measurement time to 8 sec to record two successive PSDs.

-
- [1] J. R. Johansson, P. D. Nation, and F. Nori, *Computer Physics Communications* **183**, 1760 (2012).